

An Automated Inverse Method to Calibrate Thermal Finite Element Models for Numerical Welding Applications

T. R. Walker, C. J. Bennett

*Gas Turbine and Transmissions Research Centre, Faculty of Engineering, University of
Nottingham, University Park, Nottingham, NG7 2RD, UK*

Abstract

Numerical modelling of welding processes is often completed using a sequentially coupled FE thermo-mechanical analysis to predict both the thermal and mechanical effects induced by the process. The accuracy of the predicted residual stresses and distortions are highly dependent upon an accurate representation of the thermal field. Utilising this approach, the physics of the melt pool are replaced with a heat source model which represents the heat flux distribution of the process. Many heat source models exist; however, the parameters which define the geometrical distribution have to be calibrated using experimental data. Currently the most common method involves trial and error, until the predicted thermal history and melt pool geometry accurately represent the experimental data. Although this is a simple approach, it is often time dependant and inherently inaccurate. Therefore, this study presents an automated calibration process, which determines the optimum element size for the FE mesh and then refines the parameters of the heat source model using an inverse approach. The proposed procedure was implemented for laser beam welding, operating in both the conductive and keyhole regimes. To ensure that both the thermal history data and melt pool geometry were predicted with accuracy, a multi-objective optimisation was required. The proposed methodology was experimentally validated through welding nine IN718 samples using a Nd:YAG laser heat source. A good correlation between the experimental and numerical data sets were apparent. With regards to the predicted melt pool geometry, the maximum error for the width, depth and area of the melt pool was 8.4%, 4.0% and 11.0% respectively. The minimum error was 1.5%, 0.3% and 0.3% respectively. For the temperature profiles, the maximum and minimum error for the peak temperature was 8.6% and 1.2%. Overall, the proposed calibration procedure allows automation of an

important step in the thermal modelling of welding process, allowing a more efficient industrial use of the sequentially coupled FE approach.

Keywords: Welding; Finite Element; Heat Source Model; Calibration; Automated Analysis; Optimisation

Nomenclature

ρ	Material density
C_p	Specific heat capacity
T	Temperature
t	Time
Q	Internal heat generation rate
∇	Spatial gradient operator
\vec{q}	Heat flux vector
η	Process efficiency
P	Laser power
r_s	Gaussian heat source radius
r_c	Cylindrical heat source radius
h_c	Height of the cylindrical heat source
h_{bed}	Thermal contact conductance coefficient
f	Heat flux partition factor
x, y, z	Cartesian coordinates
e_1, e_2	FE mesh element size 1 and 2
T_j^{e1}, T_j^{e2}	Discrete temperatures within the temperature profile
$f(\mathbf{x})$	Global optimisation function
\mathbf{x}_0	Optimisation vector
\mathbf{x}	Initial guess vector
$\mathbf{x}_u, \mathbf{x}_l$	Upper and lower bounds of the optimisation
w	Weight parameter
T_k^{exp}, T_k^{pre}	Experimental and predicted temperature for discrete data point k
W_m^{exp}, W_m^{pre}	Experimental and predicted melt pool width for discrete data point m
K, M	Total number of data points in each objective function
n	Total number of data points in the FE thermal history and melt pool geometry
i	Current time step of the analysis
T_m	Melting temperature of the material
W	Melt pool width
D	Melt pool depth
τ	Thickness of the workpiece

1. Introduction

The accurate prediction of the thermally induced residual stresses and the associated distortions from welding, utilising the Finite Element (FE) method, is highly dependent on the accuracy of the simulated thermal field [1]. Analytical models can be used to determine the thermal distributions of the process [2]–[5]; however, these approaches often only provide quasi-static solutions for simplified geometries. Numerical analysis provides a more realistic prediction of the thermal field, as the heating and cooling phase can be determined for the weld process; therefore, allowing the subsequent thermo-mechanical effects to be investigated. A common approach for welding simulations is to use a sequentially coupled thermo-mechanical FE model [6]. This method replaces the complex physical phenomena within the melt pool and the heat flux distribution with an equivalent FE heat source model.

A number of different heat source models exist with the Gaussian disc [7], cylindrical [8] and double ellipsoid [9] models being the most common. Heat source models can either be applied to a single surface of the geometry or to the entire volumetric domain depending on the welding process and the associated heat flux distribution. Often, the heat source model is selected depending on the type of welding process used and for some cases, two or more models are superimposed [10]–[12]. This is required to model complex flux distributions present in Electron Beam Welding (EBW) and in keyhole laser welding. For all heat source models, a number of parameters have to be quantified before it can be implemented within a FE model. Also, the process efficiency and secondary heat losses should be included as these affect the prediction of the thermal history cycle of the process. The parameters of the thermal model have to be calibrated to ensure that the temperature distributions and subsequent melt pool geometry are represented with accuracy. Often an initial guess of each parameter is obtained based on physical measurements of the weld pool geometry and from previously published values. The parameters are then refined using a manual trial and error approach until the predicted temperature profile and fusion zone represent experimental measurements. Although this method is most commonly used due to its simplicity, it is often very time consuming and inaccurate. To reduce the error between the predicted thermal field and melt pool geometry, a fully automated approach would be beneficial. It should be noted that currently, the literature surrounding this topic is limited.

A study presented by Azar *et al.* [13], utilised an analytical approach presented by Myhr and Grong [14] to determine the geometrical parameters of a double ellipsoid heat source model. The calibration was completed using isotherms from the model to determine the fusion zone. A numerical FE model was used to verify the accuracy of the heat source parameters by comparing the analytical and numerical weld pool shape, with a maximum error of 16.44% and 0.87% for the melt pool width and length respectively. It should be

noted that no attempt was made to determine the heat source parameters based on experimental data, as the aim of the study was to correlate the analytical and numerical approach; however, a major benefit of this method was the fast computational speed of the analytical methodology, allowing the parameters to be determined in approximately 2 seconds. Wu *et al.* [15], [16] calibrated an analytical 3D thermal welding model through the use of experimental measurements. The aim was to calibrate both the melt pool geometry and thermal field by obtaining two adjustment ratios which are used to modify the analytical thermal field. The major benefit of the approach was the reduction in computational time from implementing an analytical methodology; however, the approach was limited as the method cannot be extended for different heat source models and the thermal field could not be used to derive a sequentially coupled FE model. Fu *et al.* [17] also used an analytical approach to define the parameters of a double ellipsoid heat source model. A neural network was trained based on the Levenberg-Marquardt algorithm to allow the heat source parameters to be determined. Evaluation of the calibration methodology was completed by comparing experimental temperature profiles to ones derived using a transient thermal FE model. A good agreement was attained between the predicted and experimental temperature profiles, with a maximum error for the peak temperature equating 5%; however, the predicted cooling rate was underestimated by the FE model as the secondary heat losses were not included. It should be noted that the experimental melt pool geometry was also not included in the calibration methodology, therefore, a true representation of the melt pool may not have been achieved. Another calibration approach, using the Levenberg-Marquardt algorithm, was presented by Rouquette *et al.* [18]. The method aimed to quantify the effective power, beam diameter and the source position of a Gaussian energy distribution, representing an electron beam heat source. A 2D quasi-steady state model was used to predict the thermal fields of the process, with the parameters being determined based on an inverse approach. The methodology was extensive as a sensitivity analysis was required to determine the effect of each parameter on the final temperature field. The profile of the fusion zone was not included in the validation of the calibration method, nor was it used to determine the heat source parameters. It was therefore determined that the temperature measurements alone do not allow for the beam diameter to be determined using the Levenberg-Marquardt algorithm. From comparing the experimental and predicted thermal field, the maximum error for the peak temperatures was 6.97% and for some cases the cooling rate was overestimated. An automated solution procedure was presented by Belitzki *et al.* [19], which utilised optimisation algorithms to define the geometrical parameters of a double ellipsoid heat source. The welding process was assumed to be quasi-stationary with a constant weld geometry. The temperature histories were neglected from the optimisation procedure, therefore only a single objective optimisation was used. Overall, a good

agreement between the experimental and predicted fusion zone was achieved from the optimisation. A maximum error of 8.9% and 4.4% was achieved for the width and depth of the melt pool respectively; however, due to the requirement of multiple optimisation algorithms, the approach was computationally intensive. Also, no attempt at determining the process efficiency or secondary heat losses was included. Although methods to calibrate thermal FE models exist, they are limited to a single heat source model. They are also only calibrated using either a single temperature history profile or melt pool geometry; therefore, the thermal model may not have been fully calibrated. It should be noted that no attempt was made to determine a suitable element size for the previous numerical models used for calibration. A sufficient element size should be used which provides a solution independent of the mesh for the temperature field and subsequent melt pool geometry. Belitzki *et al.* [19] conducted a brief mesh independence study for a manually calibrated heat source; however, the final element size was used for the subsequent optimisations, with no attempt to verify the initial element size when using the optimised result. An automated mesh refinement model for 3D FE simulation of welding was presented by Lindgren *et al.* [20]. The model refined the mesh area in the area of the HAZ to model the non-linear thermal effects at the heat source. The refinement was based on a graded hexahedral element using the h-adaptive method; however, no attempt was made to measure the error of the solution based on physical quantities such as the temperature or melt pool area. It should be noted that no attempt to define the parameters of the heat source was completed during this study; therefore, a complete calibration of the thermal model was not achieved.

Determining the process efficiency and secondary heat effects of welding process using numerical and experimental investigations has received some attention in the literature. Often, to represent the secondary heat losses, a thermal contact conductance coefficient is included on the surface in contact with welding apparatus. Some authors [21]–[23] determine both of these parameters through trial and error until the thermal field and melt pool geometry match experimental data; however, methods to determine these values through numerical/experimental investigations exist within the literature. Ganser *et al.* [24] used a numerical CFD model to determine the process efficiency for a deep penetration weld. The numerical model was calibrated using a step wise method until the isotherm representing the melt pool geometry matched the experimental case. The process efficiency was then calculated by determining the absorbed power within the keyhole and comparing this to the original input power of the heat source. Although the method to determine the process efficiency based on an inverse approach was valid, the accuracy of this parameter was dependent upon the heat source parameters, which were determined through trial and error. Also, the predicted thermal histories were not compared to thermal data, therefore the effect of the process efficiency on the peak temperature was not

evaluated. Salerno *et al.* [25] combined an experimental and numerical approach to determine the process efficiency for TIG welding. The parameters of the heat source model and the element size were not determined as part of this study. Experimental samples were fabricated which were isolated and in contact with the welding apparatus. A trial and error approach was required to determine the process efficiency utilising a numerical FE model, with the secondary heat losses determined through modification of this parameter. The calibration of the process efficiency was evaluated for the thermal history and melt pool geometry with a maximum error of 6.6% and 14.2% respectively. It should be noted that the predicted geometry of the melt pool profile for some cases did not reflect the experimental micrograph, this was due to incomplete calibration of the FE heat source model. Although a relatively simple method to determine both the process efficiency and secondary heat losses was presented, the trial and error approach was not an effective method to quantify the variables of the thermal model. To date, methods to predict the secondary heat loss are limited within the literature. Ayoola *et al.* [26] presented an analytical method to evaluate the proportion of energy dissipated through conduction into the bulk material. An analytical representation of the thermal field was used to generate an isotherm to represent the fusion zone. From, this the energy loss was determined through integration of each temperature interval from the melting temperature to ambient. This method gives an indication of the energy losses through conduction; however, it would be difficult to determine the exact losses to the welding apparatus. Also, no method is presented to include this energy loss within a thermal FE model. From the review of the literature, methods to determine the process efficiency and secondary heating losses are limited; therefore, these phenomena must be implemented within the calibration procedure to ensure the thermal model is fully calibrated.

The validity of the current calibration methods need to be investigated as both the thermal history and melt pool geometry were not considered to calibrate the model parameters. Also, no attempt was made to determine the process efficiency, heat source parameters and the effect of secondary heat losses from the domain; therefore, a complete calibration of the thermal model was not achieved. The previous approaches are also limited as they are restricted to a single heat source model. For the previous numerical calibrations mesh independence was not addressed, as this would be a factor in the accuracy of the predicted thermal fields, it should be included in the thermal calibration. In response, this study presents a fully automated calibration procedure which determines: the optimum element size for the Heat Affected Zone (HAZ), the parameters of the FE heat source model, the process efficiency and the thermal losses associated between the workpiece and the welding apparatus. The calibration process implements the trust-region reflective algorithm to determine the parameters of the thermal model. An investigation is present to determine if a single or multi-objective function optimisation was required. The

calibration procedure was validated experimentally for a laser heat source, operating in both the conductive and keyhole regime. The model incorporated a hybrid heat source consisting of a Gaussian disc and cylindrical model, to allow the complex flux distribution of each regime to be included. Experimental thermal histories and melt pool geometries were obtained for a range of process parameters and were compared against the calibrated results. Overall, the proposed calibration procedure allows automation of a key step in the thermal modelling of welding processes; therefore, increasing the efficiency of the sequentially coupled FE approach for industrial application.

2. Methodology

A novel methodology is presented which determines the optimum element size and the parameters of a thermal FE model. The calibration procedure was designed to include any combination of heat source model, thus allowing the calibration to be applied to common welding processes. The model determines the optimum element size and refines the parameters of the thermal model to determine a calibrated set of results. To develop the methodology, convergence criteria at key stages of the process were determined through parametric studies which are presented as part of this work. Also the validity of the approach to refine the thermal model parameters was also investigated when a single-objective optimisation (SOO) or a multi-objective optimisation (MOO) was used.

The proposed method was validated using experimental test cases which were fabricated using laser beam welding (LBW). A range of process parameters were used across the entire process window for the current experimental set up.

2.1 Thermal Model Calibration Methodology

The calibration procedure, presented in Figure 1, can be divided into two sections; the first determines the optimum element size for the thermal solution, based on an initial guess for the parameters of the thermal model. The second refines the parameters using an iterative optimisation algorithm. To initiate the calibration, an initial guess for the thermal model parameters was required. These parameters were stored in the initial guess vector denoted, \mathbf{x}_0 . The element size was determined through the use of a fully automated mesh sensitivity study and converged when the thermal history and melt pool area complied with a predefined convergence criteria. The thermal model parameters were then refined using a non-linear optimisation, based on the trust-region reflective algorithm. To ensure that the final optimised solution was mesh independent, the accuracy of the thermal history and melt pool profile were reassessed. If the convergence criteria was not achieved, the optimisation was repeated utilising the new element size and the current optimised

parameters. The calibration procedure was terminated when both mesh independence was achieved and when the current and previously optimised heat source parameters were within an acceptable tolerance.

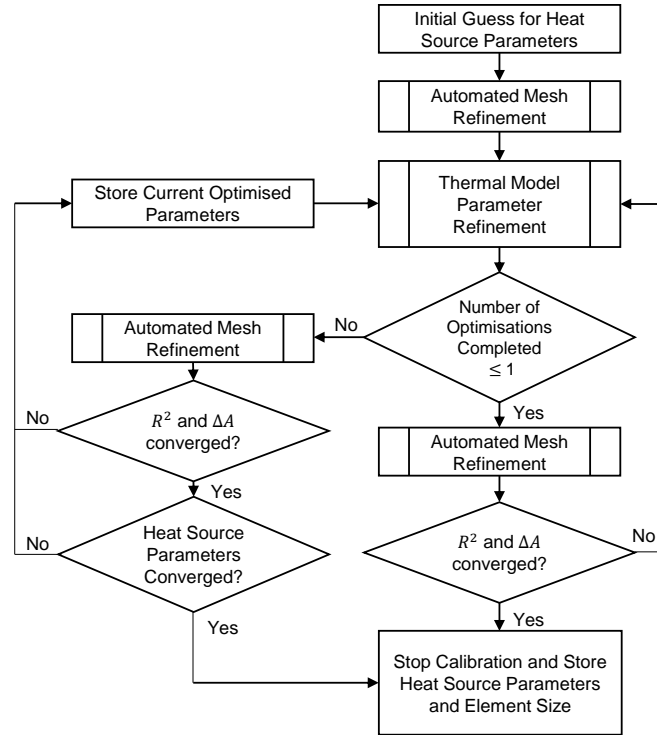


Figure 1 Flowchart of the calibration procedure used to determine the optimum element size and the parameters of the thermal model.

2.1.1 Thermal Model Theory

To determine the thermal history and melt pool profile, an underlying numerical model was utilised. A thermal FE heat transfer analysis was used to solve the transient heat conduction equation which had the form:

$$\rho C_p \frac{\partial T}{\partial t}(x, y, z, t) = -\nabla \cdot \vec{q}(x, y, z, t) + Q(x, y, z, t) \quad (1)$$

The commercial FE code ABAQUS was used to solve the transient thermal fields for all of the numerical models. The FE domain was solved using the full Newton-Raphson integration scheme, with an integration time step equalling the time required for the heat source to move one element length. The geometry and the associated weld path that was used for the thermal model is presented in Figure 2.

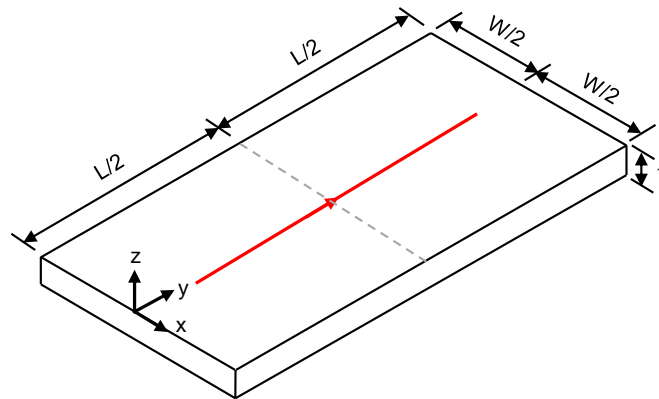


Figure 2 Schematic of the geometry and weld path used for the underlying thermal model. Thermal history data taken at mid plane highlighted with the grey dotted line.

Only the heating phase of the weld cycle was considered; therefore, a fixed time increment was used throughout the entire analysis. Due to the symmetric geometry and the associated temperature field, only half of the workpiece was modelled. The convective and radiative losses were considered using the Newton and Stefan-Boltzmann laws respectively. These boundary conditions were applied to all of the free surfaces. To include the thermal losses due to the workpiece being in contact with the welding apparatus, a thermal contact conductance coefficient was applied to the bottom of the workpiece. It should be noted that to determine this parameter, the cooling portion of the thermal history was required. To generate this data from the thermal model, the thermal history was extracted at the mid plane of the weld path ($y=50$ mm); therefore, allowing the cooling phenomena to be represented.

The domain was meshed using 8 node linear brick elements (DC3D8), with the mesh consisting of square element volumes throughout. Due to the high thermal gradients within the vicinity of the heat source, finer elements were used in this region. Through the use of mesh biasing, the element size far field was ten times the element size in the HAZ. The through thickness element size equated the finer element size. Temperature dependant material properties were included in the thermal model and the effects due to solidification of the melt pool were included using the latent heat of melting at the respective solidus and liquidus temperatures.

2.1.2 Automated Mesh Refinement

The initial stage of the procedure determined an optimum element size which satisfied the initial guess vector. The flowchart of the process used to determine the element size is presented in Figure 3. The geometry of the workpiece was meshed with an element size in the HAZ equating the size of the maximum half width of the experimental melt pool. A heat

transfer model was completed for one time step to determine the current temperature profile and melt pool geometry. Each sequential time step was then evaluated using the *Restart* function within ABAQUS. The iterative FE model was terminated when a steady state melt pool was achieved. This was implemented to reduce the computational time of the analysis. For each time step of the heat transfer analysis, the location at which the melt pool area was at its maximum was determined. The through thickness isotherm (x-z plane) at this location was used to determine the melt pool geometry, where the coordinates were defined by:

$$\begin{aligned} T(W, 0, 0) &= T_m \\ T(0, 0, D) &= T_m \end{aligned} \quad (2)$$

If no melting occurred for the current time step, the width of the melt pool was set to zero for the entire depth of the workpiece. For the current time step, a steady-state melt pool was achieved if the following criteria were satisfied:

$$\left(\frac{W_i - W_{i-1}}{W_i} \right) \leq 0.005 \quad (3)$$

$$\left(\frac{D_i - D_{i-1}}{D_i} \right) \leq 0.005$$

The selected convergence value was based on the work by Ahsan *et al.* [27]. The steady-state melt pool geometry was stored for the current element size in conjunction with a thermal profile which was determined from a predefined path along the centre of the weld path. For the next iteration of the model, the element size was reduced by 50% to determine a second melt pool geometry and temperature profile.

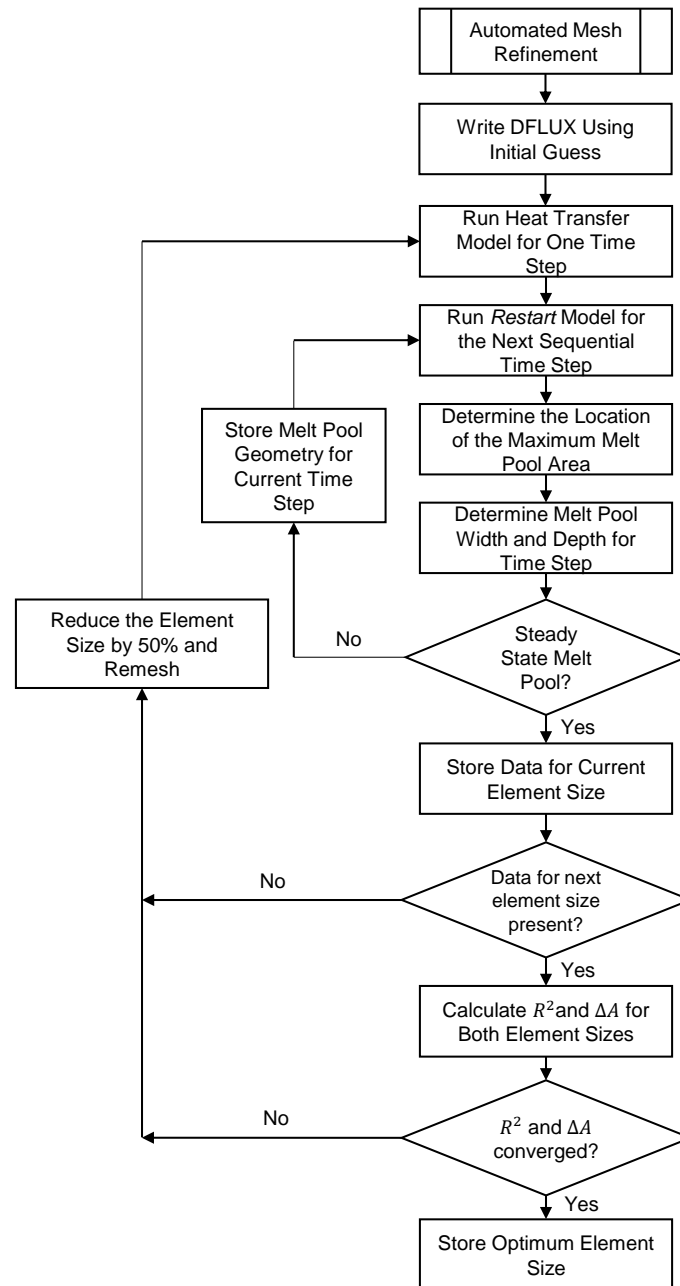


Figure 3 Flowchart of the process used to determine the optimum element size for the initial thermal model parameters.

The accuracy of the two sets of results were compared by calculating the coefficient of determination (R^2) between the temperature profiles and the change in melt pool area. The change in melt pool area was selected as it was previously found that complete mesh independence was not achieved when using only the thermal field [28]. Also as the melt pool area was being used within the optimisation, a more robust mesh could be determined using the melt pool area compared to using solely temperature data for the mesh study. The coefficient of determination (R^2) was calculated as follows:

$$R^2 = \frac{\sum_{j=1}^n (T_j^{e_1} - T_j^{e_2})^2}{\sum_{j=1}^n \left(T_j^{e_1} - \frac{1}{n} \sum_{j=1}^n T_j^{e_1} \right)^2} \quad (4)$$

To allow a consistent comparison to be made for each element size, the number of data points in each profile had to be equal. To achieve this, the data set containing the fewer data points was linearly interpolated; therefore, only one point was predicted within two data points. The melt pool area was calculated using the trapezoidal integration scheme as follows:

$$A_{melt} = W_{max} \tau - \frac{1}{2} \sum_{j=1}^{n-1} [x_{j+1} - x_j] [z_j + z_{j+1}] \quad (5)$$

Upon the convergence criteria being met, the optimum element size was stored in conjunction with the meshed FE domain which was used for the thermal model parameter refinement.

During the thermal model parameter refinement, the element size was not changed from the initial determined value. This was due to the formulation of the optimisation algorithm, as a mesh independence check could not be performed for each iteration of the optimisation. Also, if this was possible, the overall computational deficit would be costly due to the number of thermal analyses required. Therefore, it was assumed that the initial mesh size was satisfactory for all of the subsequent iterations of the thermal model parameter refinement. After an optimised set of thermal model parameters was determined, mesh independence for this solution was checked. This was completed by meshing the geometry using an element size 50% less than the initial value. The process outlined in Figure 3 was then utilised, using the same convergence criteria. If the convergence criteria was met for the current optimised parameters, the calibration procedure was terminated; however, if the convergence criteria was not met, the optimisation was repeated for the new element size which achieved mesh independence. Upon determining another set of optimised parameters, the percentage difference between each heat source parameter was calculated. If the value was less than the prescribed convergence criteria, the calibration process was terminated; however, if the criteria was not achieved, the mesh refinement and optimisation model were repeated.

2.1.3 Thermal Model Parameter Refinement

The thermal model parameters, which included the geometrical parameters of the heat source, the process efficiency and the thermal contact conductance coefficient, were determined using an inverse analysis approach. The inverse approach minimised the error

between the experimental and predicted numerical data, with the process outlined in Figure 4. A schematic of the inverse approach is presented in Figure 5.

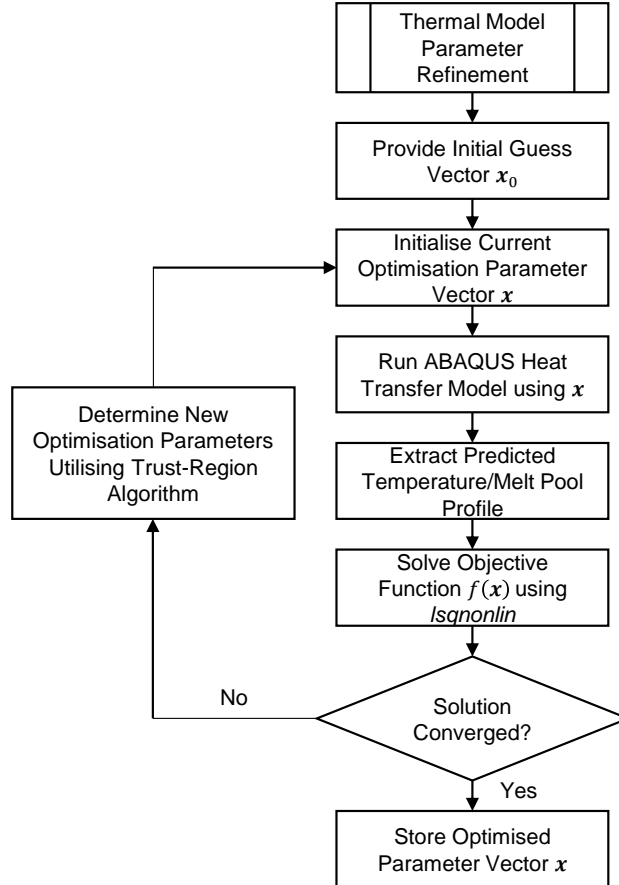


Figure 4 Flowchart of the inverse analysis used to determine the parameters of the thermal model.

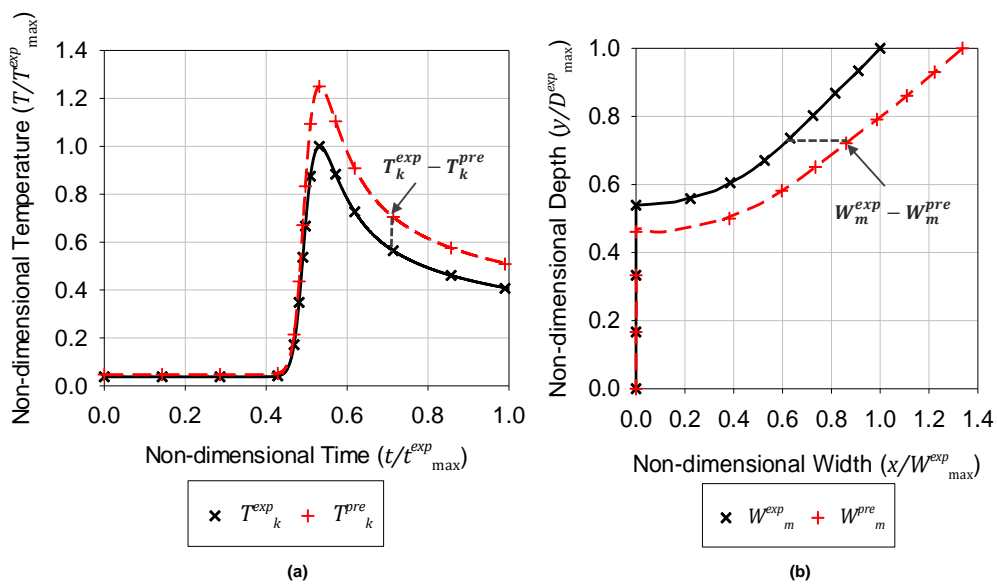


Figure 5 Schematic of the inverse approach for (a) Calculating the residual error for the thermal profile and (b) Calculating the residual error for the melt pool geometry.

The data used for the optimisation was the through thickness steady-state melt pool geometry and a thermal history profile. To minimise the error between the two data sets, a non-linear optimisation using the trust-region reflective algorithm, based on the work by Coleman and Li [29], was utilised. The algorithm minimises the squared 2-norm of the residual error, which is computed by the objective function, $f(\mathbf{x})$. It is proposed for this study, that a MOO was required, therefore two objective functions ($f_1(\mathbf{x})$ and $f_2(\mathbf{x})$) were defined. The validity of this approach was assessed as part of this study. The global objective function was calculated using the weighted sum approach [30] and had the following form:

$$f(\mathbf{x}) = \begin{bmatrix} f_1(\mathbf{x}) \\ f_2(\mathbf{x}) \end{bmatrix}^2 \quad (6)$$

$$f_1(\mathbf{x}) = \frac{w}{T_{max}^{exp}} \sum_{k=1}^K [T_k^{exp} - T_k^{pre}] \quad (8a)$$

$$f_2(\mathbf{x}) = \frac{(1-w)}{W_{max}^{exp}} \sum_{m=1}^M [W_m^{exp} - W_m^{pre}] \quad (8b)$$

The optimisation vector contained the thermal model parameters which need to be refined. This vector was bound by an upper and lower limit based on the physical constraints of the problem. A bound model was used to restrict the solution space of the optimisation, which increased the rate of convergence and minimised the non-uniqueness of the solution. For this study, the upper and lower bound were determined from the physical constraints of the problem.

The optimisation algorithm was implemented using the inbuilt MATLAB function *lsqnonlin*. Using the initial guess, the heat transfer model was used to predict the melt pool geometry and temperature history profile for the current set of thermal model parameters. These points can be denoted as a vector, \mathbf{x} , in space. The FE model was evaluated for the entire weld path outlined in Figure 2. The melt pool profile was determined from the x-z planar isotherm at the mid length of the plate, at the time step where the melt pool area was at a maximum value. It should be noted that each objective function was non-dimensionalised with respect to the maximum corresponding experimental value. This ensured that the difference in magnitude between the two objective functions did not bias the error contribution to the global objective function.

During the evaluation of the optimisation algorithm, multiple variants of the thermal parameters are evaluated for each iteration of the algorithm. Therefore, the melt pool geometry will have a varying cross-sectional profile, which could range from a partial to a full penetration profile. To ensure that the residual error was calculated at the sample point

m , regardless of the melt pool geometry, M data points were equispaced through the thickness of the workpiece. If no melting was present, the width was assigned a value of zero for the corresponding depth. To compute the residual error, both the experimental and predicted data were linearly interpolated, to ensure that the objective function was evaluated at the specific points k and m respectively. It should be noted that the total number of data points in each objective function was governed by the experimental temperature data collection. An equal number of data points was selected for both objective functions to ensure that the contribution of error to each function was not weighted due to an uneven number of data points [19].

2.2 Implementation of the Thermal Calibration

For the current study, the procedure was implemented for LBW. As the energy density available was higher than conventional arc welding (10^{10} W/m² compared to 10^8 W/m² [31]), the laser beam can operate in both the conductive and keyhole regime [31]; therefore, the geometry of the melt pool can range from a shallow elliptical shape with a low penetration depth in the conductive regime [32] to a narrow, parallel sided geometry, with a deep penetration depth in the keyhole regime [33]–[35]. This is often referred to as the nail head geometry. The process parameters used for this study encapsulated the entire process parameter window for the current experimental set up.

2.2.2 Experimental Methods

Nine samples were fabricated using the process parameters presented in Table 1, with the experimental set up presented in Figure 6. The specimen geometry was 100 x 50 x 6 mm. No filler material was used during the fabrication of the test samples. The workpiece material was IN718 with the chemical composition presented in Table 2. The material was supplied by Haynes International (Manchester UK.) in the solution heat treated state. Prior to welding, the material was sand-blasted to reduce its reflectivity. A 2 kW Ytterbium doped, continuous wave, fibre laser (IPG photonics), operating at a wavelength of 1070 nm was used. To prevent rigid body motion of the samples during fabrication, four restraining bolts were positioned along the width and the length of the workpiece. No other clamping mechanisms were used. After the weld pass was completed, the specimens were cooled in air to room temperature.

Table 1 Process parameters used for the experimental validation of the calibration procedure.

Parameter Set	Power (W)	Traverse Velocity (mm/min)
1	1800	400
2	1350	400
3	900	400
4	1800	250
5	1350	250
6	900	250
7	1800	100
8	1350	100
9	900	100

Table 2 Chemical composition of IN718 in wt%.

Ni	Co	Fe	Cr	Co+Ta	Mo	Mn	Si	Ti	Al	C	B
52	1	19	18	5	3	0.35	0.35	0.9	0.5	0.05	0.004

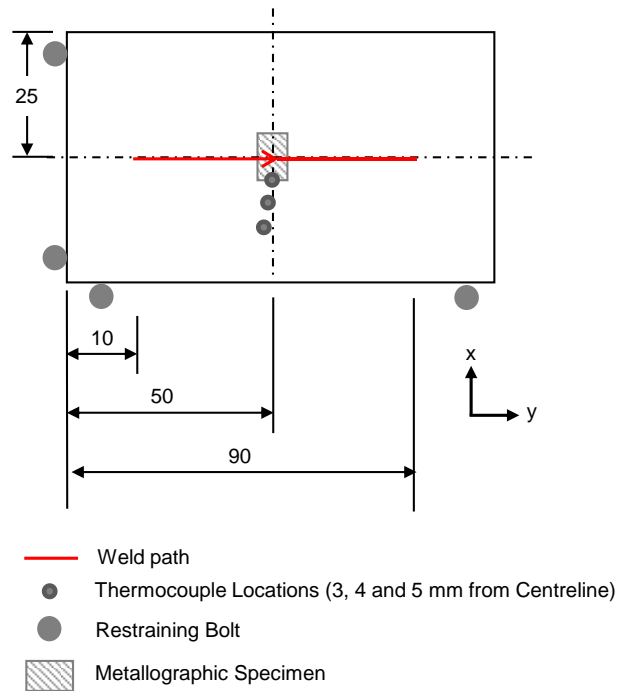


Figure 6 Schematic of the experimental set up showing the weld path, thermocouple locations and the extracted sample location for metallographic examination.

For each sample, a total of 3 in-situ temperature measurements were recorded in the region of the HAZ. K-type thermocouples, with a wire diameter of 0.3 mm, were spot welded in an open junction arrangement to the upper surface of the workpiece at the mid length ($y=50$ mm), as shown in Figure 6. After the centre of the heat source passes this position, data was still collected, up until the end of the weld path to generate the cooling data. Data was captured using a National Instruments SCXI-1000 chassis in conjunction with a SCXI-1102B voltage input module.

To determine the cross-sectional melt pool profile, metallographic examination was performed on specimens (20 x 10 x 6 mm) removed from the workpieces using waterjet cutting, as outlined in Figure 6. Each specimen was mounted in conductive resin and the exposed surface was ground using abrasive paper ranging from 250 μm to 1200 μm and then polished to a mirror finish, using a 6 μm and 1 μm abrasive diamond paste. To differentiate between the fusion line and the workpiece, each specimen was chemically etched using Beraha's tint (100 ml HCL, 50 ml H₂O, 1 g K₂S₂O₅, 1 g FeCl₃) which was swabbed onto the surface for approximately 60 seconds. A micrograph image was taken using an optical microscope. To implement the optimisation procedure, the coordinates (x , z) of the melt pool geometries were extracted from the micrographs using an edge detection algorithm implemented from the Image Processing Toolbox™ within MATLAB [36]. The cross sectional micrographs obtained from the experimental test cases are presented in Figure 7, where it can be seen that the range of parameters studied has resulted in melt pools generated by both the conductive and keyhole regimes, as the geometry of the melt pools reflect the characteristics described by Okon *et al.* [32].

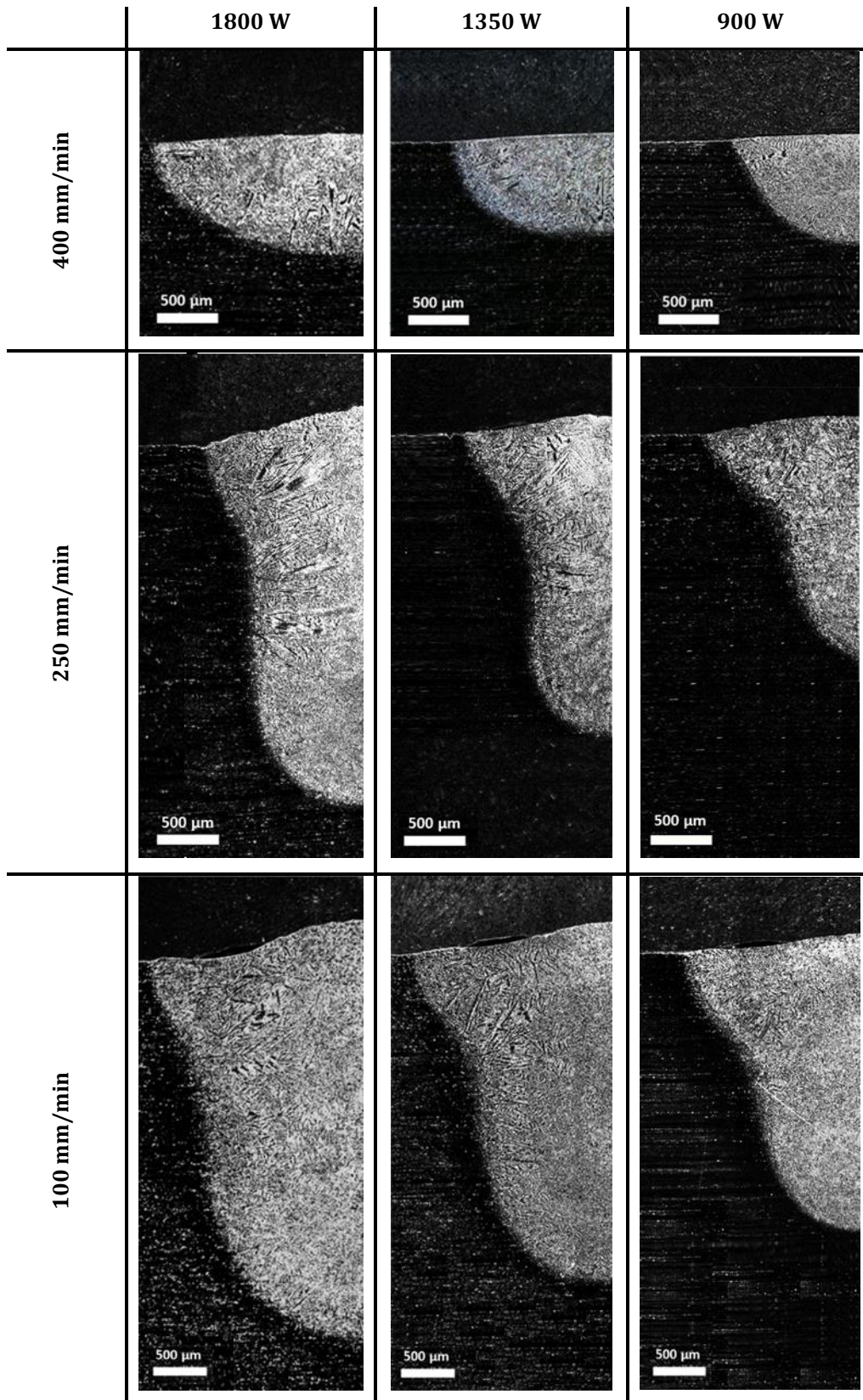


Figure 7 Cross sectional micrographs obtained from the experimental test cases for the process parameters used in this study.

2.2.2 Heat Source and Material Model

To allow the melt pool geometries in Figure 7 to be generated, the superposition of a Gaussian disc and a cylindrical heat source model was used [10]. The heat source model (Figure 8) had the following form:

$$Q_{total} = fQ_{disc} + (1 - f)Q_{cylindrical} \quad (7)$$

$$Q_{disc} = \frac{\eta P}{\pi r_s^2} \exp\left(-\frac{x^2 + y^2}{r_s^2}\right)$$

$$Q_{cylindrical} = \frac{3\eta P}{\pi 4r_c^2 h_c} \exp\left(-\frac{3(x^2 + y^2)}{r(z)^2}\right) \quad -h_c \leq z \leq 0$$

$$r(z) = r_c - \frac{z}{h_c}$$

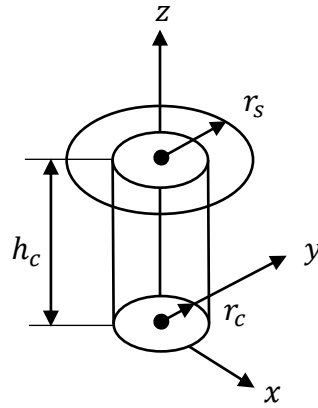
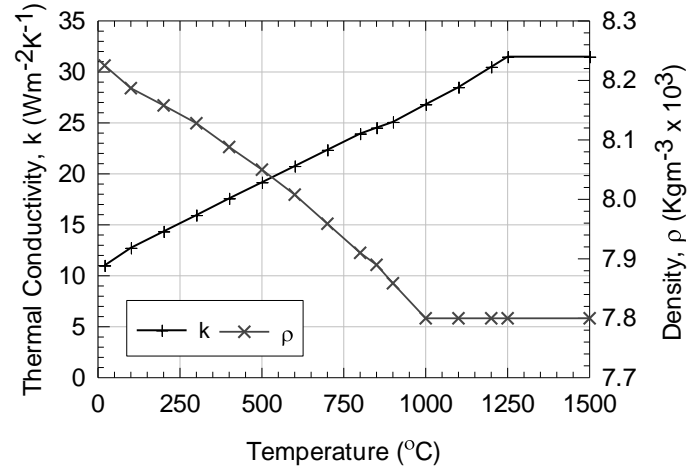
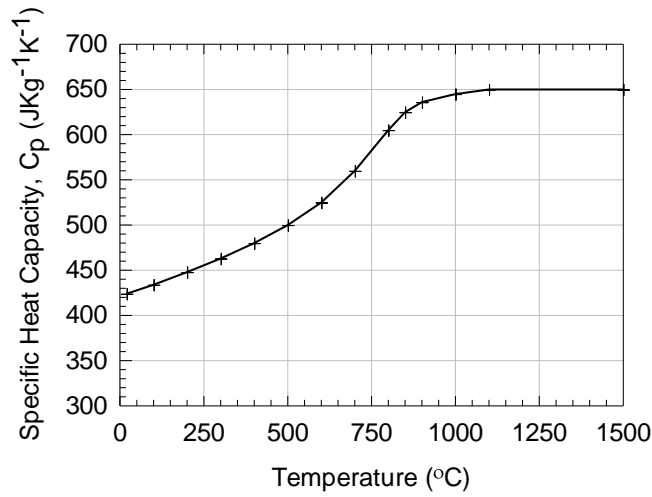


Figure 8 Schematic of the hybrid heat source model with the associated geometrical parameters.

To ensure that all regimes and melt pool geometries can be calibrated using the outlined process, the hybrid heat source model was implemented to increase the flexibility of the approach; therefore, no previous identification of the laser operating regime was required. The workpiece material selected for this study was IN718. The convective heat transfer coefficient and emissivity were set to 25 W/m²K and 0.8 respectively [37]. Temperature dependant material properties [37] were utilised in all of the numerical models as presented in Figure 9. The thermal effects, due to solidification of the melt pool, were included by applying the latent heat of melting (210 J/kg) for the respective solidus (1260°C) and liquidus (1336°C) temperatures [38].



(a)



(b)

Figure 9 Temperature dependant thermal properties of IN718 used for all FE models [37]
(a) Thermal conductivity, k , and density, ρ **(b)** Specific heat capacity, C_p .

2.2.3 Initiation of the Thermal Calibration

To initiate the thermal model calibration, an initial guess of the parameters were required. The initial guess vector for this study had the following form:

$$\mathbf{x}_0 = [r_s, r_c, h_c, f, \eta, h_{bed}] \quad (8)$$

Belitzki *et al.* [19] determined that the initial guess, supplied to a gradient based optimisation algorithm, severely effects the final optimised results. This is because several local optima can exist for the same melt pool geometry. As an alternative to using arbitrary starting values, as implemented by Belitzki *et al.* [19], the initial guess vector for this study

was determined based on physical measurements of the experimental melt pool geometry. The following assumptions were made to derive the initial guess vector for both operating regimes, with Figure 10 outlining the assumptions used to determine the geometrical parameters of the heat source:

a) Process Efficiency (η)

For both regimes, this was assumed to equal the absorptivity coefficient of IN718 and was therefore set to 0.3 [39].

b) Heat flux partition factor (f)

For the conductive regime, it was assumed that the cylindrical portion of the heat source model was not required. This was due to the shallow penetration depth; therefore, f was set to 1. For the keyhole regime, due to the complex heat flux distribution, the value was set to 0.25. This was based on the work by Ducharme *et al.* [40] and Xia *et al.* [10].

c) Gaussian radius (r_g)

An average value of the melt pool width was used in the conductive regime and for a keyhole geometry with no narrow section. If the geometry was a nail head, the parameter equated the average width between the inflection point and the penetration depth.

d) Cylindrical radius (r_c)

This parameter was equal to the Gaussian radius for both the conductive and keyhole regime with no narrow weld profile. For a nail head geometry, this parameter was equal to the width of the melt pool at the start of the narrow section.

e) Height of the cylindrical distribution (h_c)

For both regimes, this was assumed to equal the penetration depth of the melt pool geometry.

f) Thermal contact conductance coefficient (h_{bed})

For both regimes, this was set as the free surface value of 25 W/m²K as a better approximation of this value could not be achieved.

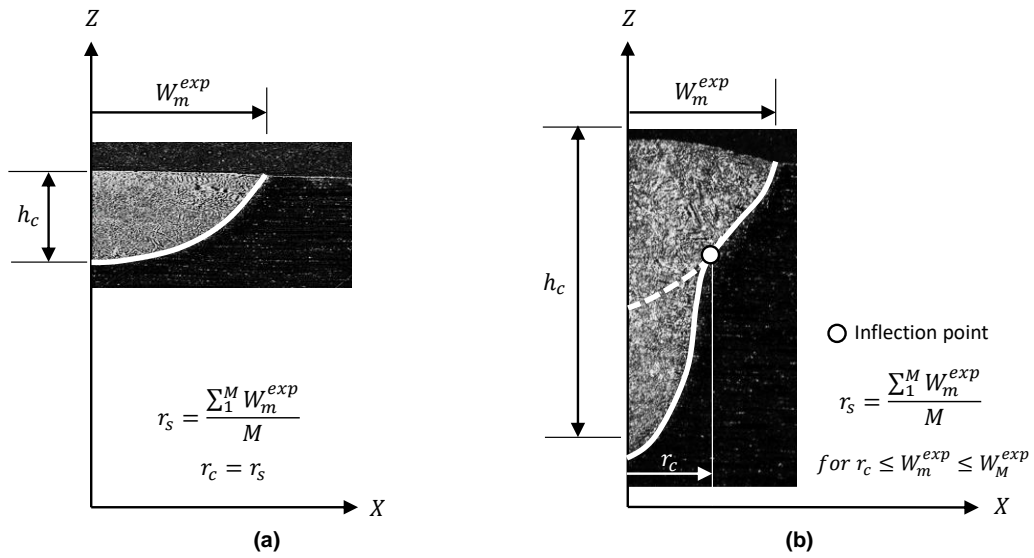


Figure 10 Schematic of the geometry used to define the initial guess for the heat source parameters for (a) The conductive and keyhole regime where no narrow section of the weld was present (b) The keyhole regime where a narrow weld section was present.

The setup of all the FE models for the calibration procedure was automated; therefore, the dimensions of the workpiece and the process parameters for the weld were specified as scalar variables at the start of the analysis. As a bound solution was utilised for the optimisation algorithm, upper and lower limits on the thermal parameters were required. The values and assumptions used to determine the bounds of the optimisation were as follows:

- a) Process Efficiency (η)

The upper and lower bound of the process efficiency were selected as 0.25 and 0.75 respectively. These values are based on the maximum and minimum energy transfer efficiency of laser beam welding, for the conductive and keyhole regime, as documented by [31].
- b) Heat Source Partition Factor (f)

The upper and lower bound was set to 0 and 1 respectively to include/not include the cylindrical heat source.
- c) Gaussian Radius (r_s)

The minimum value was assumed to equal the minimum focused spot radius of the laser, which for this current experimental set up was 0.5 mm [41]. The upper bound was equal to the maximum experimentally measured melt pool width (2.2 mm).
- d) Cylindrical Radius (r_c)

For this parameter, the lower bound was set to zero and for consistency, the upper bound was equal to the maximum Gaussian radius.

e) Cylinder Height (h_c)

The upper and lower bounds were set to 0 mm and 6 mm to reflect the maximum and minimum penetration depth of the weld geometry.

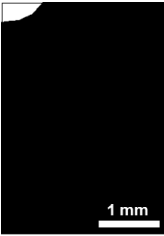
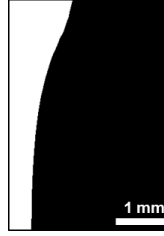
f) Thermal Contact Conductance Coefficient (h_{bed})

The lower bound for this parameter was chosen to equate the free surface value of $25 \text{ W/m}^2\text{K}$ for IN718 [37]. Due to the higher rate of heat exchange between the work piece and the welding apparatus [23], a higher magnitude value of $2000 \text{ W/m}^2\text{K}$ was used for the upper bound.

2.2.4 Determining Convergence Criteria

To determine a baseline value for the minimum allowable change in the melt pool area and an acceptable value for the coefficient of determination (R^2) determined from the temperature profile, a parametric study was conducted. For the current process parameter window (Table 3), a prediction of the melt pool geometry and thermal profile was conducted for element sizes ranging between 2 mm and 0.125 mm. The process parameter window was selected based on the work by Abioye *et al.* [42]. For each reduction in mesh size, the coefficient of determination (eq.6), the change in melt pool area (eq.7.) and the computational time required to complete the analysis were calculated. The final convergence value was selected based on a trade-off between the increase in the solution accuracy from reducing the element size and the time required for the analysis to complete. To estimate the heat flux entering the domain for the parametric study, the radii of both heat sources were assumed to equal 1.0 mm [41]. The remaining heat source parameters were determined based on the assumptions outlined in section 2.2.3. It should be noted that a higher process efficiency was required to achieve a full penetration weld profile, when the power was equal to 900 W.

Table 3 Thermal model parameters and a schematic of the melt pool geometries used for the parametric study to determine the convergence criteria (Parameter set was designed from the original set 1-9). Presented melt pool geometries are for the final element size.

Assumed Model Parameter	Parameter Set					
	A1 (Conductive)	A3 (Conductive)	A7 (Partial Penetration)	A9 (Partial Penetration)	A7 (Full Penetration)	A9 (Full Penetration)
η	0.3	0.3	0.3	0.3	0.35	0.55
f	1	1	0.25	0.25	0.25	0.25
r_s (mm)	1	1	1	1	1	1
r_c (mm)	0	0	1	1	1	1
h_c (mm)	0	0	4	4	6	6
h_{bed} (W/m ² K)	25	25	25	25	25	25
Melt Pool Geometry Schematic						

For all of the trial cases, the computational time increased exponentially due to the reduction in element size. The computational time ranged from approximately 1 minute up to 3 hours for the 2 mm and 0.125 mm element size respectively. When analysing the results across all the trial cases, it is apparent that mesh independence was achieved for the temperature profile before the melt pool geometry meaning that more nodal points are required to represent the geometry of the melt pool. The melt pool area should therefore be used in conjunction with a thermal profile to ensure that complete mesh independence has been achieved. This agrees with a previous case presented by Walker *et al.* [22].

For the conductive regime (Figure 11a and Figure 11b), mesh independence was attained for a 0.5 mm element size, as no reduction in error was achieved through a further reduction in element size. Therefore, for both cases, an optimum element volume of 0.5 x 0.5 x 0.5 mm³ in the HAZ was required. The increase in the error associated with the melt pool area, observed for the case A1, was as a result of the heat flux distribution being better represented by the FE domain in subsequent iterations due to the increase in discretisation points present within the domain. Therefore, this altered the predicted thermal field and as a result, the melt pool geometry.

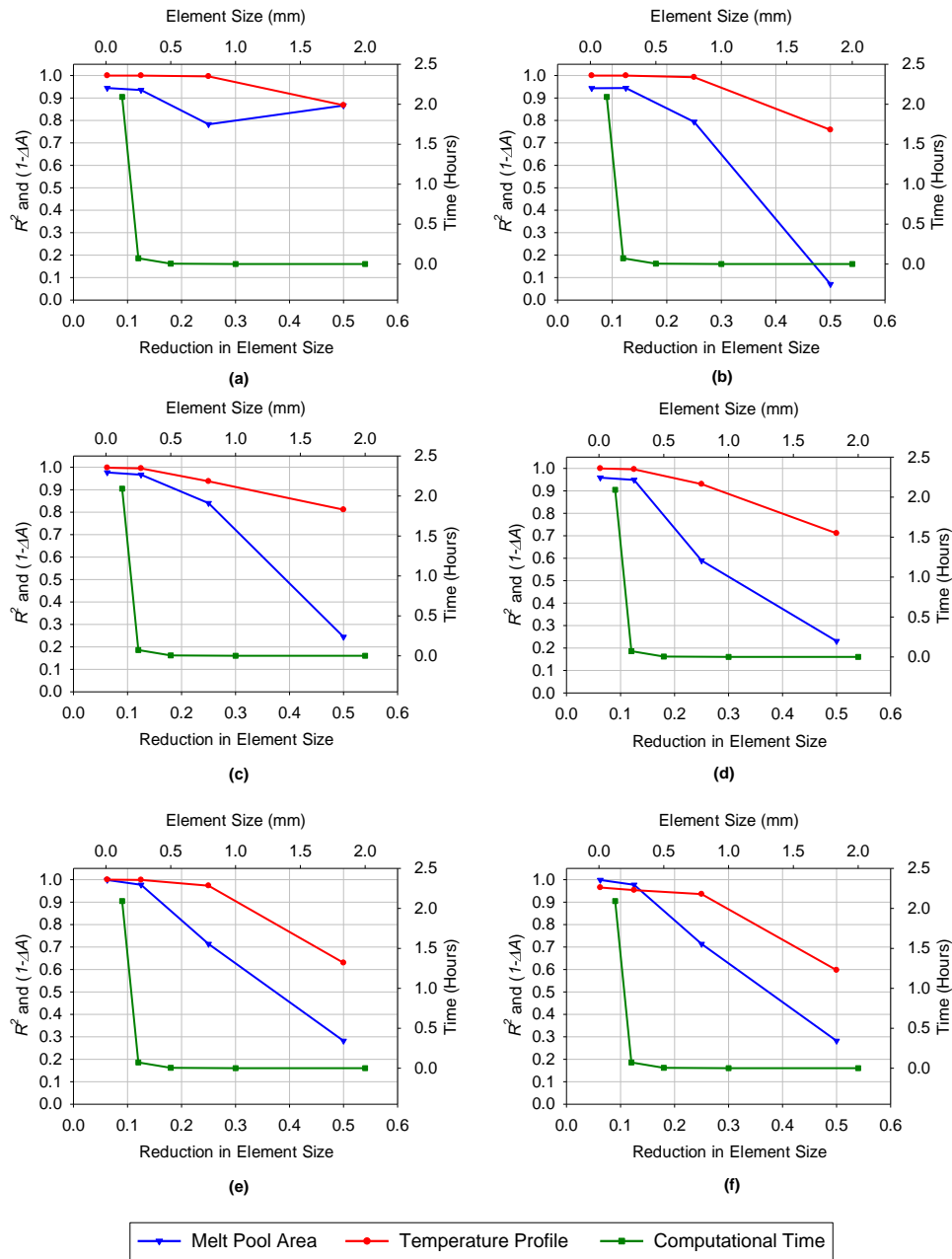


Figure 11 Results from the parametric study showing the change in melt pool area ($1 - \Delta A$) and the coefficient of determination (R^2) for each element size. (a) Set A1-Conductive (b) Set A3-Conductive (c) Set A7-Partial Penetration (d) Set A9-Partial Penetration (e) Set A7-Full Penetration (f) Case A9-Full Penetration

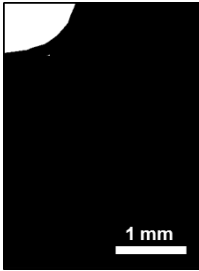
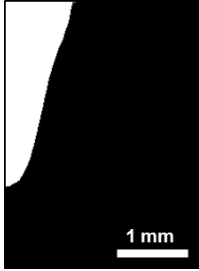
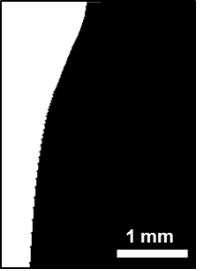
For the keyhole regime, mesh independence was not as definitive as the error between the predicted melt pool areas was still changing when reducing the element size from 0.25 to 0.125 mm. For both of the partial penetration cases, a maximum reduction in error of 1% was achieved between the melt pool geometries for a two hour increase in computational time. As no considerable reduction in error was attained for such a large computational deficit, the optimum element size was determined as 0.5 mm for both cases. As, the same phenomena was present for both of the full penetration cases, the same

element size was selected. For all of the test cases, the element size to achieve mesh independence was determined as 0.5 mm. To determine the convergence criteria for the change in melt pool area, the minimum change in this parameter, to obtain a mesh independent solution was utilised. The minimum change in melt pool area, to achieve the optimum element size (0.5 mm), for the presented cases was 6.5% (Figure 11a); therefore this value was used for the convergence criteria. For consistency, the same value was used for the coefficient of determination, for the temperature profile, i.e. $R^2 \leq 0.935$

2.2.5 Determining the Effect of w on the Solution

To determine if a multi-objective optimisation was required, the value of the weight applied to the composite objective function was varied and the effect on the solution was monitored. The weights applied to the objective function have to sum to unity when implementing a weighted sum method [30], therefore the weight (w) was varied from 0 to 1. This was completed for the test cases outlined in in Table 4, which defined a known solution for the optimisation, referred to as the target solution. It should be noted that the assumed model parameters here are different from Table 3, to ensure that three common melt pool geometries (elliptical, nail head and full penetration) were evaluated. The initial guesses were determined from the numerically derived melt pool geometries, using the same assumptions previously outlined.

Table 4 Parameters and a schematic of the melt pool geometries used for the test cases to generate the target solutions to evaluate the use of a SOO or MOO for the optimisation algorithm. (Parameter set was designed from the original set 1-9)

Assumed Model Parameter	Parameter Set		
	B1 (Conductive)	B8 (Partial Penetration)	B7 (Full Penetration)
η	0.3	0.35	0.3
f	1	0.25	0.3
r_s (mm)	1	1	1.2
r_c (mm)	0	0.9	1
h_c (mm)	0	4	6
h_{bed} (W/m ² K)	500	500	500
Melt Pool Geometry Schematic			

3. Results and Discussion

3.1 Effect of w on the Solution

To determine if a Single Objective Optimisation (SOO) or a Multi Objective Optimisation (MOO) was required, the weight parameter, w , was varied between 0 and 1. It should be noted that a w value of 0 and 1 provided a SOO based on the melt pool geometry and the temperature history respectively. The results of the parametric study are presented in Figure 12 and Table 5.

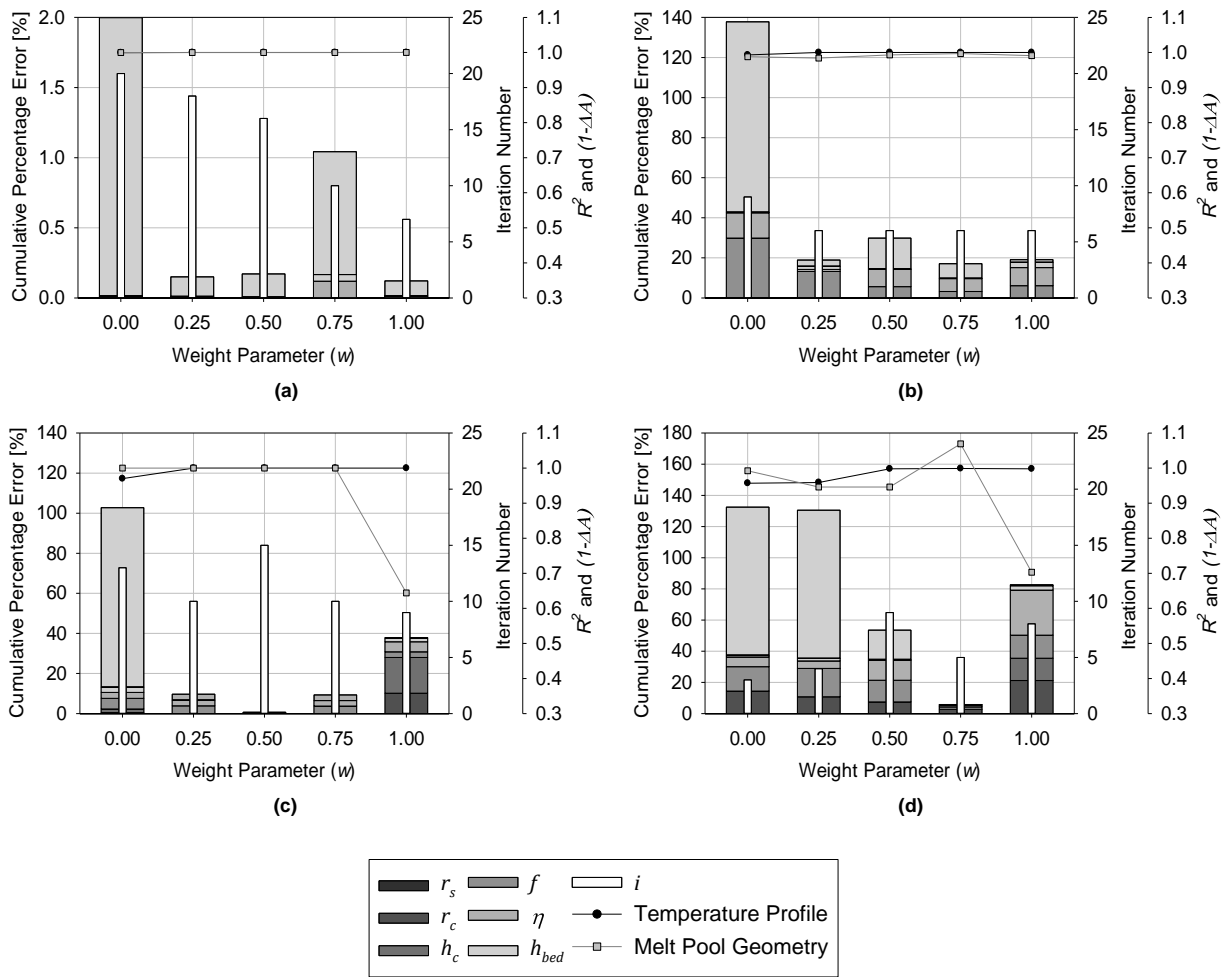


Figure 12 Cumulative percentage error between the target solution and the optimised parameters for different weight values. (a) Set B1 using Gaussian heat source only (b) Set B1 using combined heat source (c) Parameter Set B8 (d) Parameter Set B9

Table 5 Optimised parameters for the four cases used to evaluate if a SOO or MOO was required.

Parameter	Parameter Set									
	B1 (No Cylindrical Heat Source)					B1 (Hybrid Heat Source)				
	0	0.25	0.5	0.75	1	0	0.25	0.5	0.75	1
w	0	0.25	0.5	0.75	1	0	0.25	0.5	0.75	1
η	0.29	0.29	0.29	0.29	0.29	0.30	0.30	0.30	0.30	0.30
f	1	1	1	1	1	0.87	0.89	0.91	0.94	0.91
r_s (mm)	1	1	1	1	1	1.3	1.1	1.1	1.0	1.0
r_c (mm)	0	0	0	0	0	1.3	1.5	1.6	1.7	1.3
h_c (mm)	0	0	0	0	0	1.2	1.3	1.5	1.4	1.1
h_{bed} (W/m ² K)	25	499	499	496	499	25	515	422	464	507
Parameter	B8 (Hybrid Heat Source)					B9 (Hybrid Heat Source)				
	0	0.25	0.5	0.75	1	0	0.25	0.5	0.75	1
	w	0	0.25	0.5	0.75	1	0	0.25	0.5	0.75
η	0.36	0.36	0.35	0.36	0.36	0.35	0.34	0.35	0.35	0.34
f	0.24	0.24	0.25	0.24	0.24	0.28	0.29	0.26	0.30	0.21
r_s (mm)	1.0	1.0	1.0	1.0	1.1	1.4	1.3	1.3	1.2	1.5
r_c (mm)	0.9	0.9	0.9	0.9	0.7	0.9	0.8	1.1	1.0	0.9
h_c (mm)	4.2	4.2	4.0	4.1	4.1	6	6	6	6	5
h_{bed} (W/m ² K)	52	499	500	500	500	25	25	406	501	497

From the review of previous literature, authors [17]–[19] calibrated the heat source model using a SOO, considering only the temperature history or the melt pool geometry; however, from Figure 12 it is apparent that a SOO is not sufficient to calibrate the parameters of a thermal FE model. For all three cases using the hybrid heat source model, a MOO was required. When only using a SOO the maximum value of the cumulative percentage error was greater than when a combination of the two objective functions were considered. When the weight parameter was zero, i.e. a SOO for the melt pool geometry data, the parameters of the heat source were determined with accuracy; however, a high error was presented for the thermal contact conductance coefficient. This was because the optimisation algorithm had no temperature data for the cooling phase of the process. Therefore, this parameter was governed only by the thermal history data and not by the geometry of the melt pool. When the weight parameter equated one, the residual error for the thermal contact conductance coefficient was reduced due to the inclusion of the cooling phase of the process. From Figure 12, it is apparent that a SOO could be used for the conductive regime when only the Gaussian disc heat source was used, as this gave the lowest cumulative error between the target and optimised solution. This was because, for

the Gaussian disc model, only three optimisation parameters were used, with the efficiency and Gaussian radius governing the temperature history and melt pool profile. Therefore, when the optimisation algorithm varies these two parameters, the associated solution for the thermal history and melt pool geometry are coupled. This means, for this case only, the same thermal history will always generate the same melt pool geometry because of the limited variation in heat flux distribution achievable from this type of heat source model. Therefore, it is recommended that when a multi-parameter heat source model is required a MOO should be implemented. It should be noted that although the cumulative percentage error was higher when the hybrid heat source was implemented for the conductive regime, the melt pool geometry and thermal history were still represented with accuracy. This can be validated from analysing Figure 13a, Figure 13b, Figure 14a and Figure 14b, as no change in the melt pool geometry or thermal history was generated through the use of the hybrid heat source model.

From analysing Figure 14-15 in conjunction with the coefficient of determination (R^2) for the temperature profile and the change in the melt pool area ($1 - \Delta A$) from Figure 12, it is apparent that multiple variants of heat source parameters can provide the same solution for the thermal profile and the melt pool geometry. This, therefore, supports the work presented by Beltzki *et al.* [19]; however, for the fully penetrative keyhole case (Figure 12d), only one optimum solution existed and this was when the cumulative percentage error was at a minimum value. The optimum weight was selected based on the value which provided the lowest cumulative percentage error with respect to the target solution. For the conductive regime and the fully penetrative keyhole case, the optimum weight value was 0.75; however, for the partially penetrative keyhole case, the optimum value was 0.5. When the value was 0.75, the temperature profile was influencing the optimisation procedure by a ratio of approximately 3:1; however, when the weight was reduced to 0.5, the ratio was 1:1. Therefore, for the partial penetration case, an artificial reduction of each objective function was not required to provide an equal contribution of error to the global objective function; however, for the other three cases, an artificial reduction was required. To ensure that the calibration procedure can be used for any melt pool geometry and to ensure that the operating regime does not have to be pre-determined, a value 0.75 was used for w . Using this value was deemed to be valid for the partial penetration case, as the cumulative percentage error was less than the maximum value obtained for the other two operating conditions, for the same weight.

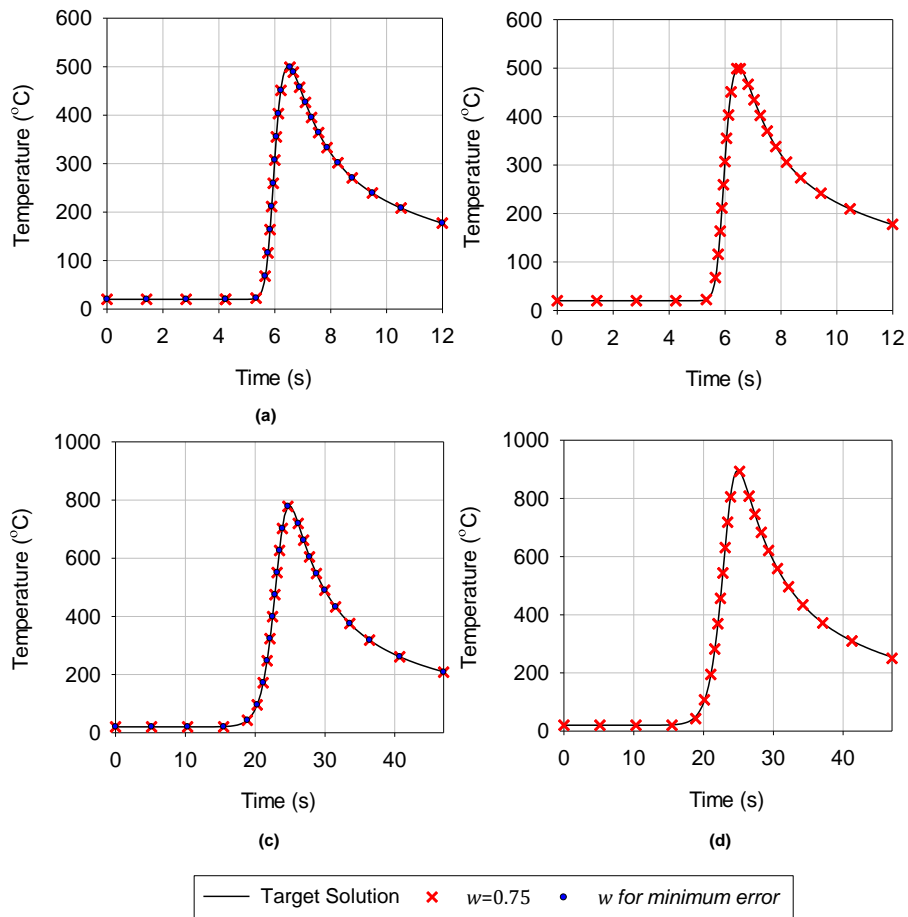


Figure 13 A plot comparing the target thermal solutions with the solution for $w=0.75$ and for w giving the minimum error (a) Set B1 no cylindrical heat source (b) Set B1 with the hybrid heat source (c) Set b7 (d) Set B8. It should be noted for (a) and (b) the optimum was for $w=0.75$.

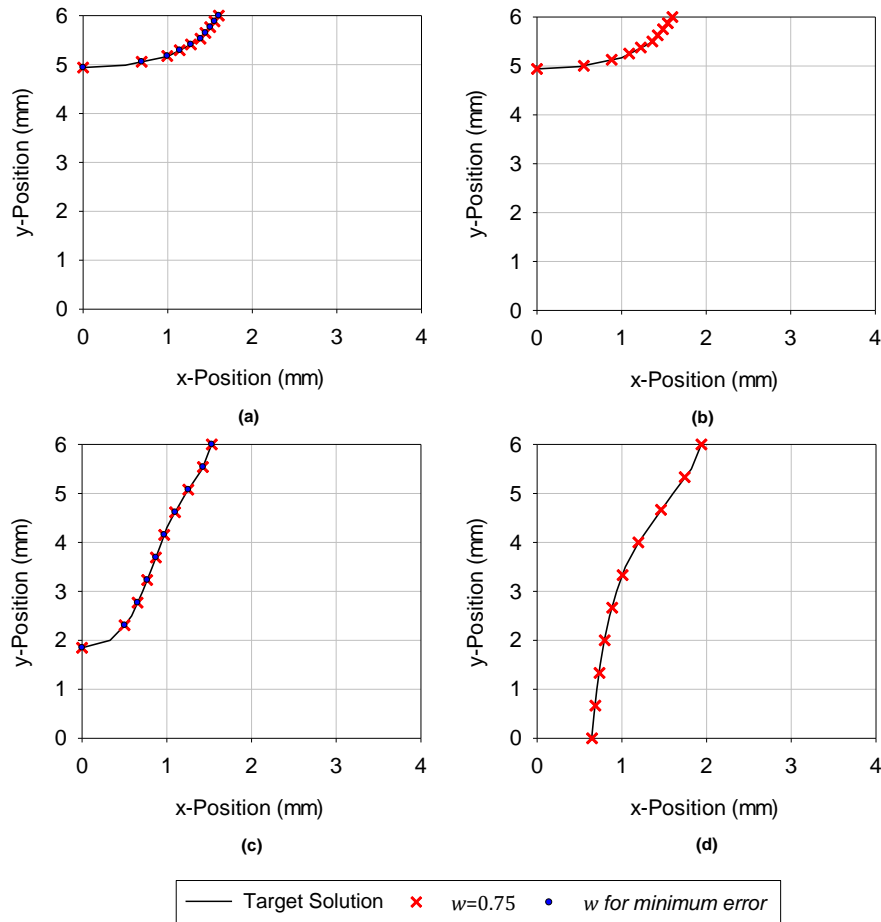


Figure 14 A plot comparing the target melt pool geometries with the solution for $w=0.75$ and for w giving the minimum error (a) Set B1 no cylindrical heat source (b) Set B1 with the hybrid heat source (c) Set b7 (d) Set B8. It should be noted for (a) and (b) the optimum was for $w=0.75$.

3.2 Calibrated Thermal Model Parameters

The proposed heat source model was calibrated for nine experimental samples across the entire process window for the current experimental set up. The initial step of the calibration involved an optimum element size being determined from the initial guess vector. The initial element size for all of the experimental cases is presented in Table 6, with an example of the melt pool geometry, determined for each element size, using the automated mesh study, being presented in Figure 15. It should be noted for the presented example, the convergence criteria for mesh independence was achieved for the 0.25 mm element size. From analysing Figure 15d and Figure 15e the selected convergence criteria was appropriate, as visually, there is minimal deviation in the shape of the melt pool geometry from the 0.25 mm and 0.125 mm element size. From Figure 15, the change in the melt pool geometry was more severe during the early stage of the mesh sensitivity study,

with the melt pool profile for the 2 mm and 1mm element size being very dissimilar to the converged solution. Therefore, this highlights the importance of completing a mesh independence study to ensure that subsequent solutions from the optimisation are accurate. Previous authors [18], [19], [43], [44] have neglected this stage from the calibration procedure. Therefore, the previous approaches may lead to an inaccurate representation of the thermal field due to mesh independence not being achieved. Across the entire process window, only two element sizes were required to achieve mesh independence (0.5 mm and 0.25 mm). From Table 6, an increased element size can be used when a larger linear energy density (P/V) was present. For the high energy density cases, the initial guess for the heat source radii were in the range of 2 mm and 0.9 mm. Therefore, a greater proportion of the domain was covered by the heat source distribution, allowing the number of discretisation points, which represented the Gaussian profile of the heat sources to be reduced. As a result, larger element sizes could be used. Although, there appears to be an apparent trend between linear energy density and element size, an anomaly was present for set 6. For this case, a smaller element size to achieve mesh independence was required than for set 8. In comparison to set 6, a more complex melt pool geometry existed for case 8; therefore, the element size was not only dictated by the linear energy density, but it was also governed by the profile of the melt pool geometry. As no definitive relationship between process parameters and the optimum element size to achieve mesh independence could be determined, it is advised that this portion of the calibration procedure is always implemented.

Upon checking if mesh independence was still achieved for the optimised parameter set, it was determined that no further refinement was needed for any of the cases. Therefore, the optimisation was not repeated for any of the presented cases.

Table 6 Initial element size for the optimisation study.

Parameter Set	Initial Element Size (mm)
1	0.5
2	0.5
3	0.25
4	0.5
5	0.25
6	0.25
7	0.5
8	0.5
9	0.25

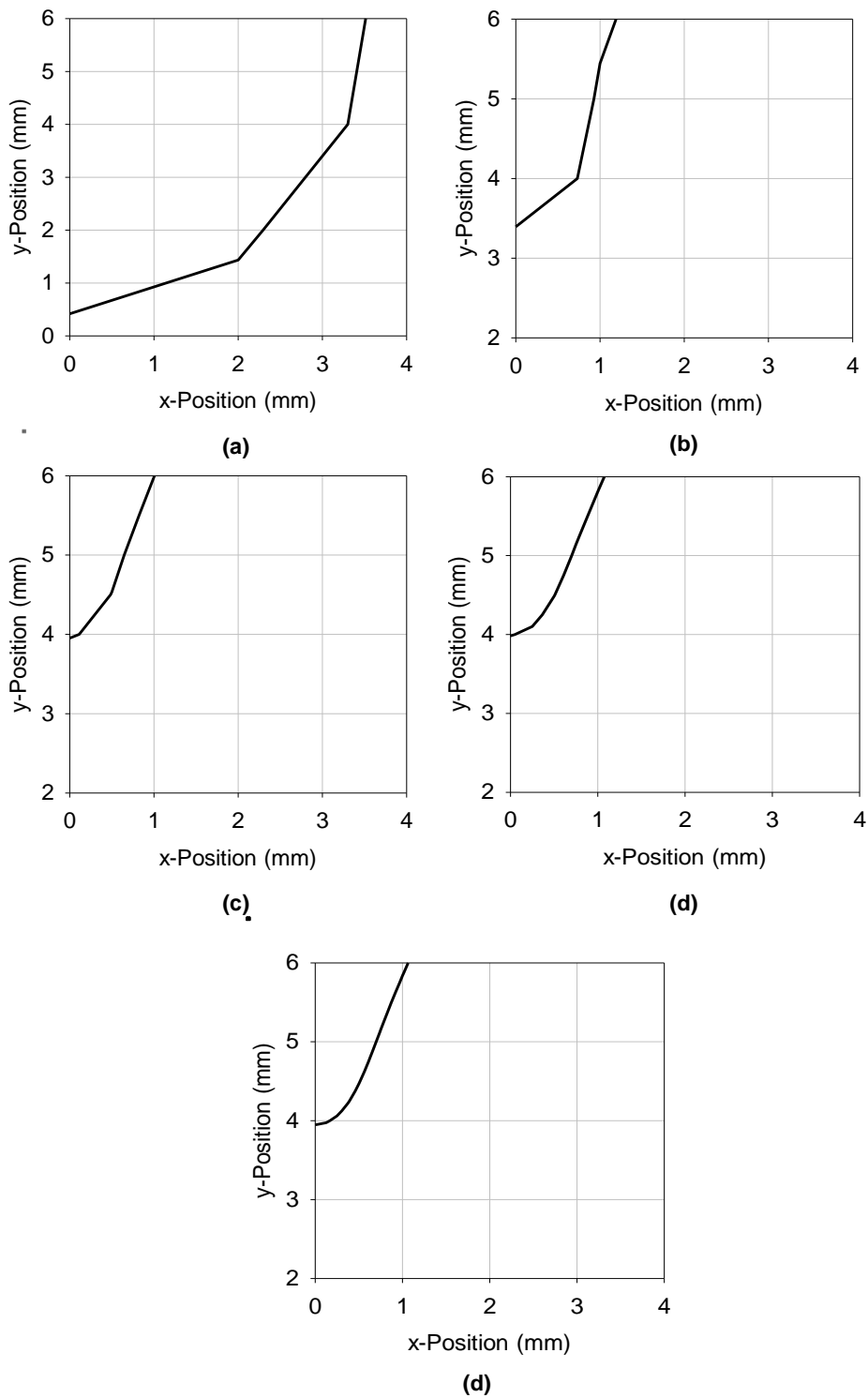


Figure 15 Example results obtained from the automated mesh sensitivity study for parameter set 9 for mesh sizes (a) 2 mm (b) 1 mm (c) 0.5 mm (d) 0.25 mm (e) 0.125 mm. The grey dots represent the nodal points of the FE domain.

The optimised thermal model parameters for all of the presented parameter sets are provided in Table 7. A comparison between the experimental and calibrated results for the thermal history and melt pool profile are presented in Figure 16 to Figure 18. It should be noted that the white profile was determined through the use of the image analysis and was used as the experimental data for the optimisation. A fair agreement was achieved between the determined profile and the experimental macrograph showing validity of the applied methodology. The error between the experimental and predicted peak temperatures for each thermocouple location is presented in Table 8. The error was also determined for key geometrical parameters of the melt pool, with the results documented in Table 9.

Table 7 Optimised heat source parameters for the combined heat source model derived using the experimental cases.

Parameter Set	η	f	r_s (mm)	r_c (mm)	h_c (mm)	h_{bed} (W/m²K)
1	0.27	0.98	1.15	0.54	1.74	25.33
2	0.29	1.00	0.89	0.87	0.73	25.00
3	0.36	0.99	0.70	0.65	0.81	25.08
4	0.39	0.17	1.81	0.54	2.86	25.16
5	0.36	0.27	1.36	0.84	2.72	25.44
6	0.38	0.50	1.28	0.38	1.86	51.17
7	0.36	0.28	1.87	1.87	3.60	181.50
8	0.35	0.19	2.00	2.00	3.02	187.48
9	0.39	0.38	1.33	0.73	2.53	344.31

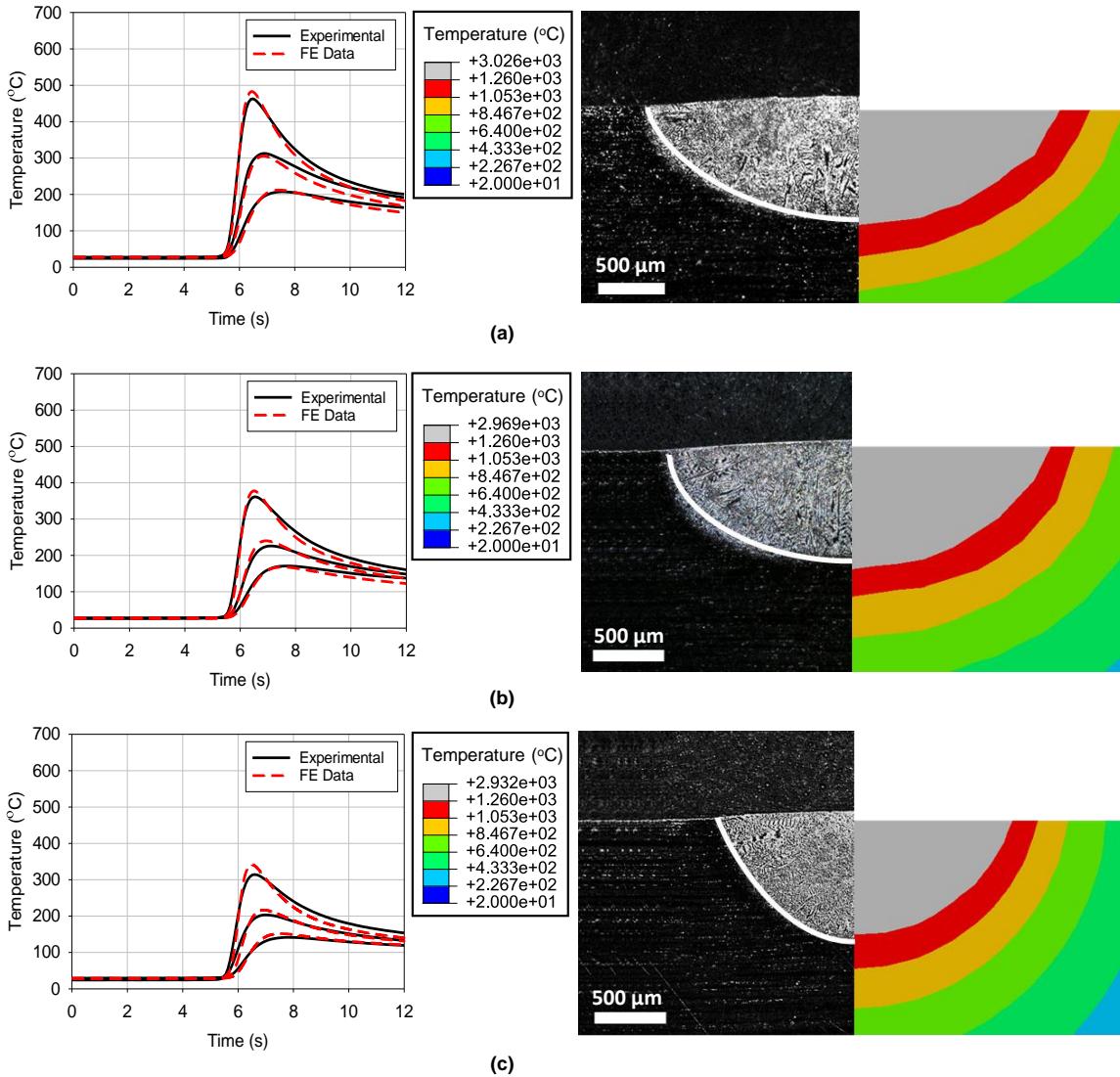
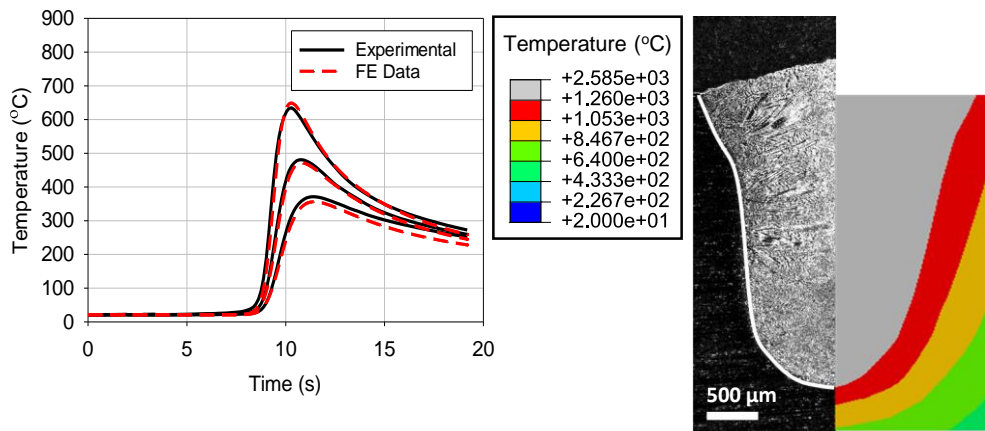
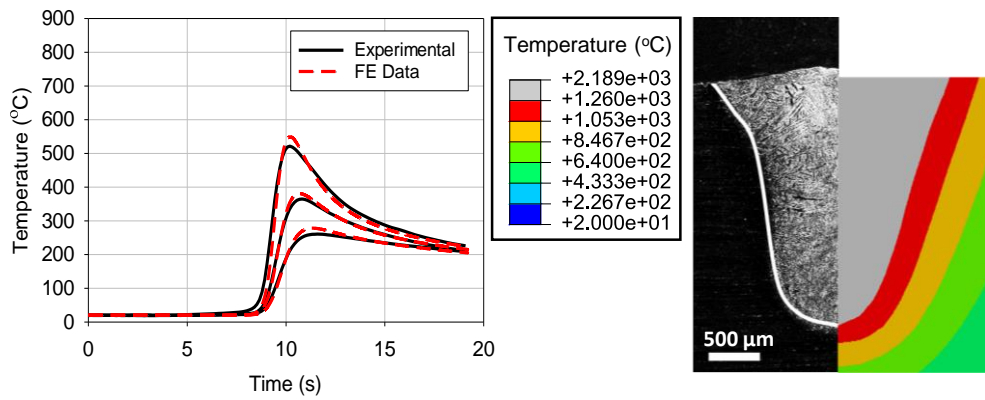


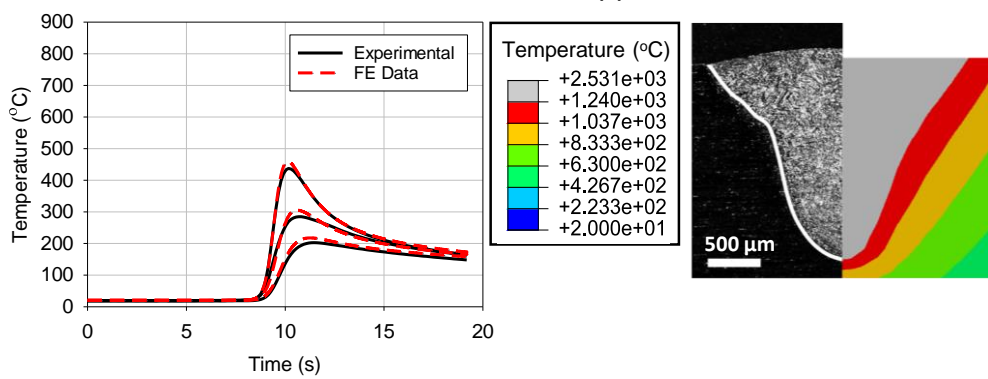
Figure 16 A comparison between the experimental and predicted thermal histories/melt pool geometries in the conductive regime for (a) Parameter set 1 (b) Parameter set 2 (c) Parameter set 3



(a)

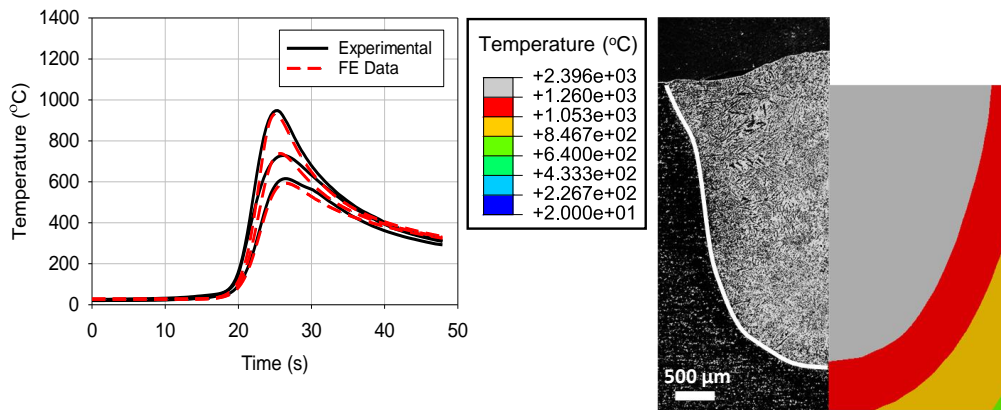


(b)

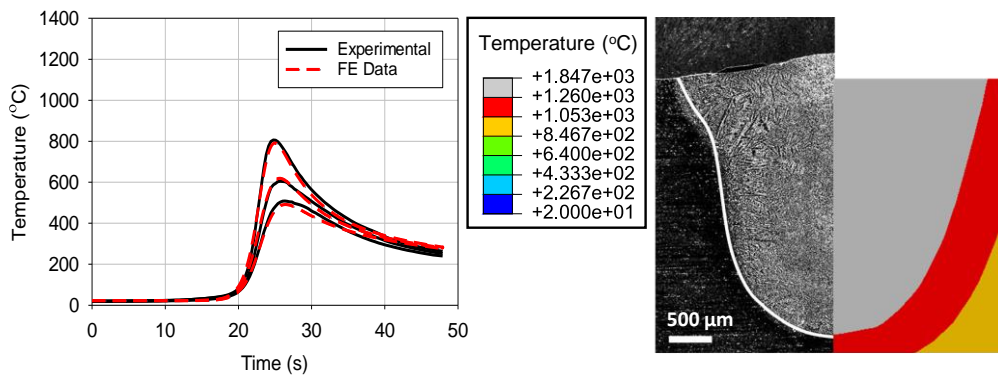


(c)

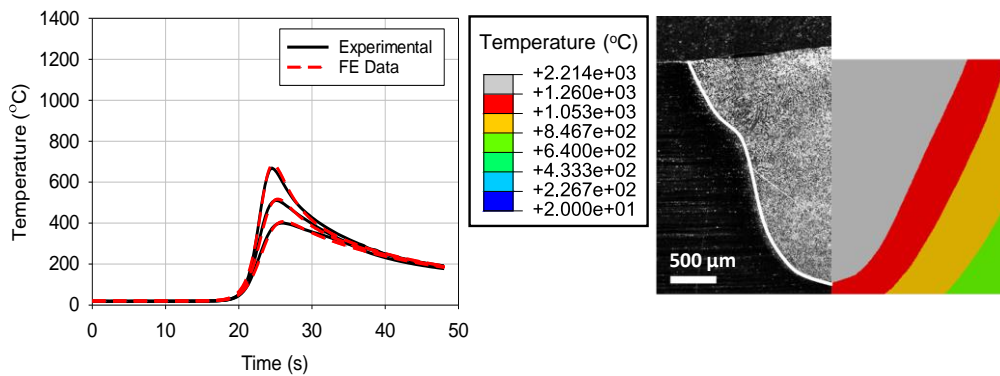
Figure 17 A comparison between the experimental and predicted thermal histories/melt pool geometries in the keyhole regime for (a) Parameter set 4 (b) Parameter set 5 (c) Parameter set 6



(a)



(b)



(c)

Figure 18 A comparison between the experimental and predicted thermal histories/melt pool geometries in the keyhole regime for (a) Parameter set 7 (b) Parameter set 8 (c) Parameter set 9

Table 8 Percentage error between the experimental and predicted peak temperature at 3 mm, 4 mm and 5 mm from the weld centreline.

Parameter Set	Percentage Error for 3 mm Peak Temperature (%)	Percentage Error for 4 mm Peak Temperature (%)	Percentage Error for 5 mm Peak Temperature (%)
1	4.3	2.2	2.2
2	4.5	6.3	1.7
3	8.6	6.5	7.1
4	2.2	2.0	4.0
5	5.3	4.4	6.7
6	4.9	7.2	7.4
7	1.8	1.3	8.3
8	1.9	2.3	3.3
9	2.6	1.2	1.8

Table 9 Percentage error between the experimental and predicted melt pool surface width (W_s), the throat width at the inflection point (W_t), the total penetration depth (D) and the melt pool area (A_{melt}).

Parameter Set	Percentage Error in W_s (%)	Percentage Error in W_t (%)	Percentage Error in D (%)	Percentage Error in A_{melt} (%)
1	4.1	N/A	3.2	3.4
2	4.7	N/A	4.0	1.0
3	8.4	N/A	3.5	11.0
4	2.2	5.8	0.8	1.8
5	8.2	1.3	2.3	4.1
6	4.6	4.6	1.4	8.1
7	1.5	14.2	3.0	9.2
8	2.2	12.8	1.6	0.3
9	6.5	2.6	0.3	6.0

For the conductive regime (parameter sets 1-3), the optimisation determined that a majority of the flux distribution was required from the Gaussian disc heat source as the heat flux partition factor was greater than 0.97 for all three sets; therefore, this determined that the Gaussian disc heat source model was appropriate for modelling the heat flux distribution for the conductive regime. For all three of these cases, the reduction in linear energy density was compensated by a reduction in the Gaussian radius (r_s), with the optimised values being less than the experimental melt pool width. Therefore, the melt

pool is predominately governed by the conduction of heat flux in the area of the HAZ. It should be noted that the parameters of the cylindrical heat source were included for this operating regime; however, the values were greater than the experimental melt pool geometry showing that the flux distribution from this heat source was negligible, as it was dissipated over a large volume. With regards to the process efficiency (η), the value determined for all three cases fell within the range of published values for the absorptivity of IN718 [39], [45]; therefore, it can be concluded that the absorption of the laser was dependent upon the surface finish of the workpiece. From Figure 16 the high thermal gradients during the heating phases were captured with accuracy for all three cases. The predicted peak temperatures agreed well for each location, with a maximum error of 8.6% for set 3. The error may occur due to a positioning error of the thermocouples, as these were positioned manually, a consistent comparison between the two data sets may not have been achieved. It should also be noted that from the FE model, a 0.25 mm change in the position of the thermal history gave rise to an 8.9% difference in the peak temperature. The error may occur due to the uncertainty in the measurements obtained using the thermocouples. Error in the thermal measurements may arise from positioning and/or systematic errors. The error analysis presented in Table 10 was completed using BS 60584 [46], with the error due to the thermocouple extension cables and NI DAQ data collection taken as $\pm 2.5^\circ\text{C}$ and $\pm 0.83^\circ\text{C}$ respectively [47]. The combined systematic error was calculated using the Root Sum of Squares (RSS) method. For the positioning error, the uncertainty in the positioning of the thermocouples equated ± 0.5 mm, with the corresponding temperature difference being determined from the FE model.

Table 10 Systematic error analysis for peak temperature measurements using BS 60584

Parameter Set	Error in TC Junction ($\pm^\circ\text{C}$)	Total Systematic Error (RSS) ($\pm^\circ\text{C}$)	Positioning Error ($\pm^\circ\text{C}$)	$T^{Exp} - T^{Pre}$ ($^\circ\text{C}$)
1	3.5	4.3	64.5	19.9
2	2.6	3.7	51.4	16.3
3	2.5	3.6	43.5	27.1
4	4.9	5.6	65.1	14.3
5	3.9	4.7	54.5	27.8
6	3.3	4.2	50.6	21.5
7	7.0	7.5	65.1	17.5
8	6.0	6.5	72.8	15.6
9	5.1	5.7	52.7	17.2

When analysing the difference between the peak experimental and predicted temperatures, the systematic error would not account for the discrepancies between the two data sets. It is apparent that the greatest error arises from positioning of the thermocouples; however, the maximum difference between the two data sets falls within the error limits showing confidence in the final solution. It should also be noted that the difference between the experimental and predicted peak temperatures, for all data sets, is less than the positioning error; therefore, the error in the position must be less than ± 0.5 mm. The thermocouple wire (0.3 mm diameter) used had a response time of 0.28 seconds was achieved; if the temperature change between room temperature and the peak temperature was assumed to be instantaneous, the minimum time taken to achieve this was 1.28 seconds; therefore, the response time would have negligible effect on the experimental data.

For the cooling phase, a fair agreement was achieved; however, an overestimate in the cooling rate was present. From Table 7, the thermal contact conductance coefficient was approximately $25 \text{ W/m}^2\text{K}$ for all of the cases in the conductive regime. This was equal to the lower bound set on the optimisation vector, \mathbf{x} . A reason for this error could be the assumption that the lower bound for this parameter equating the free surface value was incorrect or the value determined by Dye *et al.* [37] was not suitable for the current experimental set up. With regards to the melt pool geometry, the maximum error was for set 3, where the predicted melt pool geometry was overestimated. Unlike for set 1 and 2, a shallow elliptical geometry was not present for the experimental melt pool; therefore, it is apparent that the heat source model could not replicate this shape with accuracy. Due to this and the use of a MOO, a compromise between attaining an accurate thermal history and melt pool geometry was achieved. With the use of a MOO, for some cases, no improvement could be made to the global error calculated from the objective function, as a Pareto set of optimised values was obtained. When this occurred, a local minimum was achieved, even if a high magnitude of residual error was still present within the solution, therefore highlighting one drawback of this approach.

For the keyhole regime (parameter sets 4-9), a greater percentage of the heat flux distribution was required from the cylindrical portion of the heat source model. The contribution ranged from 50% to 83%; therefore, a more complex distribution of heat flux was required. The radii of the Gaussian disc and cylindrical heat source determined the final geometry of the predicted melt pool. For the parameter sets where a nail head weld profile was present (Figure 17 and Figure 18c, parameter sets 4-6 and 9), the Gaussian radius was always greater than the cylindrical radius. Therefore, the radius of the disc heat source model dictated the width of the melt pool at the surface, with the narrow section being governed by the cylindrical radius. Across sets 4 to 9, the surface width of the melt pool reduces, which was compensated through a reduction in the Gaussian radius and an

increase in the contribution from the disc heat source model. However, this compensation was not present for set 7, as the radius of the cylindrical heat source was smaller than the experimentally measured surface width. This again shows some conduction of the heat flux in the vicinity of the HAZ. The height of the cylindrical distribution was approximately equal to the total penetration depth of the melt pool for sets 4 to 9. A maximum and minimum percentage error between the height of the heat source and the experimental penetration depth was 9.3% and 0.25% respectively; therefore, showing that the assumption for the initial guess of this parameter was reasonable. It should be noted, that a large percentage error was present for the width of the melt pool for the throat of the narrow section, for set 7 and 8, as the nail head section was not predicted, with the geometry being represented as a single elliptical profile. The nail head portion does not exist as the radii of the heat source are equal, therefore a complete cylindrical distribution of the heat flux was present for these two cases. The reason why the optimisation could not determine that a nail head section was present could be due to the number of data points used to represent this geometrical characteristic. Due to the equispaced points through the thickness of the work piece, the number of data points representing the top of the nail head section would be less in comparison to the remainder of the profile. As the error contribution to the objective function would be less in comparison to the remainder of the points representing the melt pool profile, the attainable resolution for the small geometrical characteristics of the melt pool would be affected. For most of the cases in the keyhole regime, the process efficiency determined from the optimisation was greater than for the conductive regime; therefore, identifying that keyhole welding is more efficient, agreeing with [31]. However, the published values for the efficiency of a keyhole welding process range from 0.5-0.75 [31], which are greater than the values determined by the optimisation. A possible reason for this may be due to the surface finish of the work piece, as the absorption of the laser heat energy is highly dependent upon the roughness of the material [48]. Another physical phenomena causing this discrepancy maybe because the laser heat source, was not operating solely in the keyhole regime, i.e. transitioning between the conductive and keyhole regime. When calculating the peak heat flux from the optimised parameters, the maximum and minimum values were $1.18 \times 10^{11} \text{ W/m}^2\text{K}$ and $7.68 \times 10^9 \text{ W/m}^2\text{K}$ respectively. As the lower limit on the range of values was less than the published value for keyhole welding ($10^{10} \text{ W/m}^2\text{K}$ [31]), it is believed for some of the presented sets (Set 7 and 8), the weld is in a transitioning state; therefore, a lower process efficiency was determined. This can also be validated by analysing Figure 18a and Figure 18b (Parameter sets 4 and 5), where the weld geometry was predominately elliptical in shape. Therefore, the distinct geometrical features of a keyhole weld, as outlined in [33], were not present. A numerical reason for the discrepancies between the determined and published values for the process efficiency, may arise from the method in which the optimisation was reducing

the error of the objective function. The iteration history for the heat source radii and the process efficiency are presented in Figure 19. For the two cases presented, the peak heat flux equated the aforementioned upper (Figure 19a) and lower (Figure 19b) value. From analysing Figure 19, it is apparent that to minimise the objective function in early iterations of the optimisation, the solution was more sensitive to variation in the radii of the heat source. This is shown through the greater step size between the radii in comparison to the process efficiency, with a maximum percentage change of 30% and 9.3% respectively. Therefore, the process efficiency acts as a sliding scale, which was used to refine the final solution in an attempt to further reduce the error of the objective function.

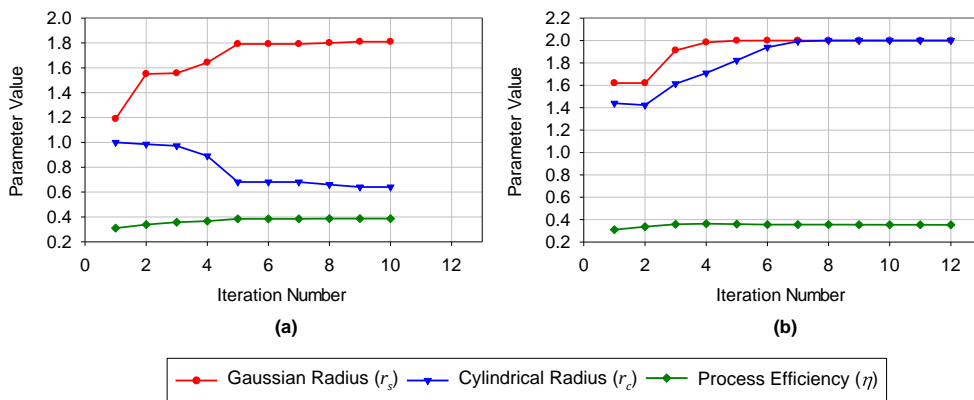


Figure 19 An example of the iteration history for the heat source radii and the process efficiency for (a) Parameter set D (b) Parameter set E.

For the predicted cooling phase of the process, a better representation of the cooling rate was achieved in the keyhole regime than for the conductive regime. It should be noted for set 4, the discrepancy in the cooling phase, for the 5 mm thermal history, was due to error in the experimental data. From Table 7, the thermal contact conductance coefficient was not dissimilar from the free surface value for sets 1-5, therefore showing that the conduction to the welding apparatus for these cases was negligible. However, for sets 6-9 the cooling rate was greater, showing that some thermal energy was lost to the bed. This increase was due to the greater penetration depth of the weld, therefore allowing heat to dissipate from the bottom surface of the workpiece. The determined values for the bed coefficient, for sets 6-9 were 6.2%, 6.5% and 12.8% higher than the free surface value, with this parameter increasing with a reduction in the applied linear energy density. To evaluate the effect of the thermal contact conductance coefficient, the cooling rate (dT/dt) was determined across the temperature range for which γ' enters solution (1150°C) and recrystallizes (1020°C) [49]. The cooling rate was evaluated for thermal contact conductance coefficient values between the upper and lower values prescribed to the optimisation. The results are presented in Figure 20. A maximum percentage increase of 4.9% was observed in the cooling rate, across the range coefficient values, showing that a

significant difference in the magnitude of the coefficient had minimal effect on the cooling rate. When comparing set 7 to 9, the maximum difference in the thermal contact conductance coefficient equated 47.4%; however, the difference in cooling rate was equal to 0.5%. The same issue can also be highlighted when comparing set 4 to 6 where a 51% increase in the coefficient value was determined which only altered the cooling rate by 0.1%. A potential reason for why a significant difference was observed, for similar process parameters, may be due to the method in which the thermal model parameters were altered during the optimisation. To calculate the step size for the next iteration of the optimisation, a quadratic sub-problem, which approximates the behaviour of the objective function, was solved [50]. For each step size, the lowest possible value of the quadratic sub-problem must be achieved, through the steepest possible decent direction, to ensure that convergence was efficient [51]. Therefore, it is believed, that for set 6 and 9, the significant increase in the thermal contact conductance coefficient was due to the optimisation solver, generating a large step size for this parameter, as this provided a more efficient convergence rate through the steepest decent method. However, as aforementioned, the large difference in the thermal contact conductance coefficient would have a negligible effect on the actual physics of the process model.

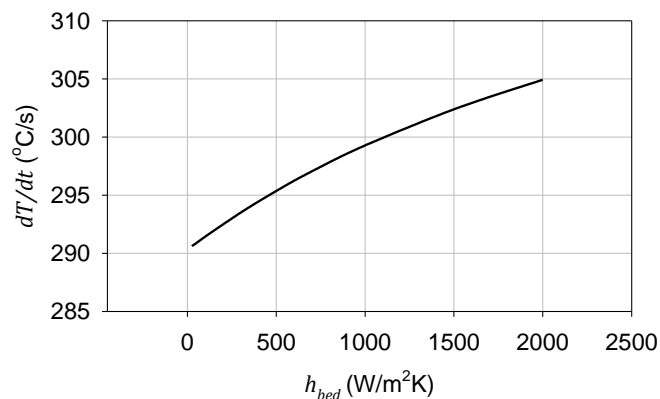


Figure 20 A graph showing the effect of the cooling rates through variation of the thermal contact conductance coefficient. The cooling rate was determined for the temperature range governing recrystallization of γ' for IN718 for $P=900$ W and $V=100$ mm/min. The thermal history data was taken from the nodal coordinate (1.5, 50, 0).

As determined from this study and the work presented by Belitzki *et al.* [19], the initial guess will dictate the accuracy of the final solution, when using gradient based optimisation techniques and in some, cases a poor initial guess may lead to divergence of the model. The reason for this is that these types of algorithm are locally convergent; therefore, a solution potentially exists, at a distant point in space, which would provide the absolute minimum response to the objective function. For the current problem, it is believed that the response from the objective function is highly non-linear, as multiple parameter sets provide an identical solution, as determined from Figure 12a to Figure 12b; therefore, there are

multiple local minima which exist on the response surface of the objective function within the selected bound constraints. When using an arbitrary guess of the heat source parameters, as completed by Belitzki *et al.* [19], a poor solution was attained, therefore a better initial guess should be provided to ensure the optimisation falls into the correct local minima. With this study, using a MOO and physical measurements of the melt pool geometry for the initial guess, a better solution was determined for the thermal model parameters; therefore, accurate calibration of the thermal FE model can be completed, automating a significant part of the sequentially coupled FE approach used to model welding processes.

4. Conclusions

A novel automated method to calibrate FE heat source models for thermal analyses has been presented and validated experimentally using LBW. The following conclusions have been identified from this work:

- Overall, the proposed calibration procedure allows automation of a key step in the thermal modelling of welding processes, therefore increasing the efficiency of the sequentially coupled FE approach for industrial application.
- The optimised parameters provide an accurate representation of both the thermal history and melt pool geometry when comparing the numerical and experimental data. The maximum and minimum error for the peak temperatures were 8.6% and 1.2% respectively. The maximum and minimum error between the predicted and experimental melt pool area was 11% and 0.3%.
- A good initial guess for the optimisation was determined through physical measurements of the experimental melt pool geometry; however, a method is required which can estimate these parameters, to ensure global convergence is achieved.
- The weighted sum method with a MOO was required to ensure an accurate solution was obtained. Future work should include determining a method to select the desired weight value without the need to use a comprehensive parametric study.
- From previous work in the literature, a SOO was used, which is appropriate for when the heat source model has one geometrical parameter which provides a coupled thermal history and melt pool geometry. For cases where the heat source model has more than one geometrical parameter a MOO should be considered.

References

- [1] U. Hartel, A. Ilin, C. Bantel, J. Gibmeier, and V. Michailov, "Finite element modeling for the structural analysis of Al-Cu laser beam welding," *Phys. Procedia*, vol. 83, pp. 1404–1414, 2016 doi:10.1016/j.phpro.2016.08.147.
- [2] H. E. Cline and T. R. Anthony, "Heat treating and melting material with a scanning laser or electron beam," *J. Appl. Phys.*, vol. 48, no. 9, pp. 3895–3900, 1977 doi:10.1063/1.324261.
- [3] A. Franco, L. Romoli, and A. Musacchio, "Modelling for predicting seam geometry in laser beam welding of stainless steel," *Int. J. Therm. Sci.*, vol. 79, pp. 194–205, 2014 doi:10.1016/j.ijthermalsci.2014.01.003.
- [4] A. Pittner, *A contribution to the solution of the inverse heat conduction problem in welding simulation*. 2012.
- [5] N. T. Nguyen, Y. W. Mai, S. Simpson, and a Ohta, "Analytical approximate solution for double ellipsoidal heat source in finite thick plate," *Weld. J.*, vol. 83, no. 3, p. 82s–93s, 2004.
- [6] L. E. Lindgren, "Numerical modelling of welding," *Comput. Methods Appl. Mech. Eng.*, vol. 195, no. 48–49, pp. 6710–6736, 2006 doi:10.1016/j.cma.2005.08.018.
- [7] V. Pavelic, R. Tanbakuchi, O. . Uyehara, and P. . Myers, "Welding Journal Research Supplement," vol. 48, pp. 295–305, 1969.
- [8] A. Evdokimov, K. Springer, N. Doynov, R. Ossenbrink, and V. Michailov, "Heat source model for laser beam welding of steel-aluminum lap joints," *Int. J. Adv. Manuf. Technol.*, no. 93, pp. 709–716, 2017 doi:10.1007/s00170-017-0569-6.
- [9] J. Goldak, A. Chakravarti, and M. Bibby, "A new finite element model for welding heat sources," *Metall. Trans. B*, vol. 15, no. 2, pp. 299–305, 1984 doi:10.1007/BF02667333.
- [10] P. Xia *et al.*, "Prediction of weld shape for fiber laser keyhole welding based on finite element analysis," *Int. J. Adv. Manuf. Technol.*, vol. 75, no. 1, pp. 363–372, 2014 doi:10.1007/s00170-014-6129-4.
- [11] Y. Liu, P. Jiang, Y. W. Ai, and C. Yue, "Prediction of weld shape for fiber laser welding based on hybrid heat source model," in *3rd International Conference on Material, Mechanical and Manufacturing Engineering*, 2015, pp. 1868–1873.
- [12] W. C. Tseng and J. N. Aoh, "Experimental Validation of a Laser Heat Source Model for Laser Melting and Laser Cladding Processes," *Open Mech. Eng. J.*, vol. 8, pp. 370–381, 2014.
- [13] A. S. Azar, S. K. Ås, and O. M. Akselsen, "Determination of welding heat source parameters from actual bead shape," *Comput. Mater. Sci.*, vol. 54, no. 1, pp. 176–182, 2012 doi:10.1016/j.commatsci.2011.10.025.
- [14] O. R. Myhr and Ø. Grong, "Dimensionless maps for heat flow analyses in fusion welding," *Acta Metall. Mater.*, vol. 38, no. 3, pp. 449–460, 1990 doi:https://doi.org/10.1016/0956-7151(90)90151-6.
- [15] S. Wu, H. Gao, W. Zhang, and Y. M. Zhang, "Analytic weld pool model calibrated by measurements - Part 1: Principles," *Weld. J.*, vol. 96, no. 6, p. 193s–202s, 2017.
- [16] S. J. Wu, H. M. Gao, W. Zhang, and Y. M. Zhang, "Measurement of calibrated recursive analytic in the gas tungsten arc weld pool model," *Weld. J.*, vol. 97, no. 4, p. 108s–119s, 2018

doi:10.29391/2018.97.010.

- [17] G. Fu, J. Gu, M. I. Lourenco, M. Duan, and S. F. Estefen, "Parameter determination of double-ellipsoidal heat source model and its application in the multi-pass welding process," *Ships Offshore Struct.*, vol. 10, no. 2, pp. 204–217, 2015 doi:10.1080/17445302.2014.937059.
- [18] S. Rouquette, J. Guo, and P. Le Masson, "Estimation of the parameters of a Gaussian heat source by the Levenberg – Marquardt method : Application to the electron beam welding," *Int. J. Therm. Sci.*, vol. 46, pp. 128–138, 2007 doi:10.1016/j.ijthermalsci.2006.04.015.
- [19] A. Belitzki, C. Marder, A. Huissel, and M. F. Zaeh, "Automated heat source calibration for the numerical simulation of laser beam welded components," *Prod. Eng.*, vol. 10, no. 2, pp. 129–136, 2016 doi:10.1007/s11740-016-0664-9.
- [20] L. E. Lindgren, H. Å. Häggblad, J. M. J. McDill, and A. S. Oddy, "Automatic remeshing for three-dimensional finite element simulation of welding," *Comput. Methods Appl. Mech. Eng.*, vol. 147, no. 3–4, pp. 401–409, 1997 doi:10.1016/S0045-7825(97)00025-X.
- [21] M. Perić, I. Garašić, Z. Tonković, T. Vuherer, S. Nižetić, and H. Dedić-Jandrek, "Numerical prediction and experimental validation of temperature and residual stress distributions in buried-arc welded thick plates," *Int. J. Energy Res.*, no. January, pp. 3590–3600, 2019 doi:10.1002/er.4506.
- [22] T. R. Walker, C. J. Bennett, T. L. Lee, and A. T. Clare, "A validated analytical-numerical modelling strategy to predict residual stresses in single-track laser deposited IN718," *Int. J. Mech. Sci.*, vol. 151, no. February 2019, pp. 609–621, 2019 doi:10.1016/j.ijmecsci.2018.12.004.
- [23] P. Foteinopoulos, A. Papacharalampopoulos, and P. Stavropoulos, "On thermal modeling of Additive Manufacturing processes," *CIRP J. Manuf. Sci. Technol.*, vol. 20, pp. 66–83, 2018 doi:10.1016/j.cirpj.2017.09.007.
- [24] A. Ganser, J. Pieper, S. Liebl, and M. F. Zaeh, "Numerical simulation of the thermal efficiency during laser deep penetration welding," in *Physics Procedia*, 2016 doi:10.1016/j.phpro.2016.08.144.
- [25] G. Salerno, C. Bennett, W. Sun, and A. Becker, "An experimental and numerical investigation on the process efficiency of the focused-tungsten inert gas welding of Inconel 718 thick plates," *J. Eng. Manuf.*, vol. 233, no. 3, pp. 823–833, 2019 doi:10.1177/0954405418775442.
- [26] W. A. Ayoola, W. J. Suder, and S. W. Williams, "Parameters controlling weld bead profile in conduction laser welding," *J. Mater. Process. Technol.*, 2017 doi:10.1016/j.jmatprotec.2017.06.026.
- [27] M. N. Ahsan and A. J. Pinkerton, "An analytical-numerical model of laser direct metal deposition track and microstructure formation," *Model. Simul. Mater. Sci. Eng.*, vol. 19, no. 5, pp. 1–22, 2011 doi:10.1088/0965-0393/19/5/055003.
- [28] T. R. Walker, C. J. Bennett, T. L. Lee, and A. T. Clare, "A validated analytical-numerical modelling strategy to predict residual stresses in single-track laser deposited IN718," *Int. J. Mech. Sci.*, vol. 151, 2019 doi:10.1016/j.ijmecsci.2018.12.004.
- [29] T. Coleman and Y. Li, "An Interior Trust Region Approach for Nonlinear Minimization Subject to Bounds," *SIAM J. Optim.*, vol. 6, no. 2, pp. 418–445, 1996 doi:10.1137/0806023.
- [30] R. T. Marler and J. S. Arora, "The weighted sum method for multi-objective optimization : new insights," no. June, 2010 doi:10.1007/s00158-009-0460-7.

- [31] R. W. Messler, "Chapter 6 - Welding as a Joining Process," in *Joining of Materials and Structures: From Pragmatic Process to Enabling Technology*, R. W. B. T.-J. of M. and S. Messler, Ed. Burlington: Butterworth-Heinemann, 2004, pp. 285–343 doi:<https://doi.org/10.1016/B978-075067757-8/50006-3>.
- [32] P. Okon, G. Dearden, K. Watkins, M. Sharp, and P. French, "Laser welding of aluminium alloy 5083," *Int. Congr. Appl. Lasers Electro-Optics*, vol. 2002, no. 1, p. 158364, Oct. 2002 doi:10.2351/1.5065620.
- [33] G. Wiklund, O. Akselsen, A. J. Sørgerd, and A. F. H. Kaplan, "Geometrical aspects of hot cracks in laser-arc hybrid welding," *J. Laser Appl.*, vol. 26, no. 1, p. 12003, Nov. 2013 doi:10.2351/1.4827135.
- [34] M. O. Gebhardt, A. Gumenyuk, and M. Rethmeier, "Numerical Analysis of Hot Cracking in Laser-Hybrid Welded Tubes," *Adv. Mater. Sci. Eng.*, vol. 2013, pp. 1–8, 2013 doi:10.1155/2013/520786.
- [35] F. Farrokhi, B. Endelt, and M. Kristiansen, "A numerical model for full and partial penetration hybrid laser welding of thick-section steels," *Opt. Laser Technol.*, vol. 111, no. September 2018, pp. 671–686, 2019 doi:10.1016/j.optlastec.2018.08.059.
- [36] R. C. Gonzalez, R. E. Woods, and S. L. Eddins, *Digital Image Processing*.
- [37] D. Dye, O. Hunziker, S. M. Roberts, and R. C. Reed, "Modeling of the mechanical effects induced by the tungsten inert-gas welding of the IN718 superalloy," *Metall. Mater. Trans. A*, vol. 32, no. 7, pp. 1713–1725, 2001 doi:10.1007/s11661-001-0149-z.
- [38] J. J. Valencia and Quested P.N, "Thermophysical Properties," *ASM Handb. Cast.*, vol. 15, no. Ref 24, pp. 468–481, 2008 doi:10.1361/asmhba0005240.
- [39] M. Anderson, R. Patwa, and Y. C. S. Ā, "Laser-assisted machining of Inconel 718 with an economic analysis," vol. 46, pp. 1879–1891, 2006 doi:<https://doi.org/10.1016/j.ijmachtools.2005.11.005>.
- [40] R. Ducharme, P. Kapadia, and J. Dowden, "A mathematical model of the defocusing of laser light above a workpiece in laser material processing," 2018, vol. 187, no. 1992, pp. 187–197 doi:10.2351/1.5058486.
- [41] P. kayode Farayibi, "Laser cladding of Ti-6Al- 4V with carbide and boride reinforcements using wire and powder feedstock," University of Nottingham, 2014.
- [42] T. E. Abioye, J. Folkes, and A. T. Clare, "A parametric study of Inconel 625 wire laser deposition," *J. Mater. Process. Technol.*, vol. 213, no. 12, pp. 2145–2151, 2013 doi:10.1016/j.jmatprotec.2013.06.007.
- [43] C. Carmignani, R. Mares, and G. Toselli, "Transient finite element analysis of deep penetration laser welding process in a singlepass butt-welded thick steel plate," *Comput. Methods Appl. Mech. Eng.*, vol. 179, no. 3, pp. 197–214, 1999 doi:[https://doi.org/10.1016/S0045-7825\(99\)00043-2](https://doi.org/10.1016/S0045-7825(99)00043-2).
- [44] K. Abdel-Tawab and A. K. Noor, "Uncertainty analysis of welding residual stress fields," *Comput. Methods Appl. Mech. Eng.*, vol. 179, no. 3–4, pp. 327–344, 1999 doi:10.1016/S0045-7825(99)00045-6.
- [45] C. SAINTE-CATHERINE, M. JEANDIN, D. KEHEMAIR, J.-P. RICAUD, and L. SABATIER, "STUDY OF DYNAMIC ABSORPTIVITY AT 10.6 μm (CO₂) AND 1.06 μm (Nd-YAG) WAVELENGTHS AS A FUNCTION OF TEMPERATURE," *J. Phys. IV Fr.*, vol. 1, no. C7, pp. C7-151-C7-157, Dec. 1991.

- [46] BSI, "BSI Standards Publication EN 60584-1:2013 Thermocouples Part 1: EMF Specifications and Tolerances," *Br. Stand.*, vol. BS EN 6058, no. 1, pp. 1–12, 2013.
- [47] J. Nakos, "Uncertainty analysis of thermocouple measurements used in normal and abnormal thermal environment experiments at Sandia's Radiant Heat Facility and Lurance Canyon Burn Site," 2004.
- [48] D. Bergström, J. Powell, and A. F. H. Kaplan, "The absorptance of steels to Nd:YLF and Nd:YAG laser light at room temperature," *Appl. Surf. Sci.*, vol. 253, no. 11, pp. 5017–5028, 2007 doi:<https://doi.org/10.1016/j.apsusc.2006.11.018>.
- [49] X. You, Y. Tan, S. Shi, J. Yang, Y. Wang, and J. Li, "Effect of solution heat treatment on the precipitation behavior and strengthening mechanisms of electron beam smelted Inconel 718 superalloy," *Mater. Sci. Eng. A*, vol. 689, no. 2, pp. 257–268, 2017 doi:[10.1016/j.msea.2017.01.093](https://doi.org/10.1016/j.msea.2017.01.093).
- [50] J. J. Moré and D. C. Sorensen, "Computing a Trust Region Step," *SIAM J. Sci. Stat. Comput.*, vol. 4, no. 3, pp. 553–572, Sep. 1983 doi:[10.1137/0904038](https://doi.org/10.1137/0904038).
- [51] R. H. Byrd, R. B. Schnabel, and G. A. Shultz, "Approximate solution of the trust region problem by minimization over two-dimensional subspaces," *Math. Program.*, vol. 40, no. 1, pp. 247–263, 1988 doi:[10.1007/BF01580735](https://doi.org/10.1007/BF01580735).